2019

Blended Wing Design Considerations for A Next Generation Commercial Aircraft

Jay Abhilash Vora
Wright State University

BLENDED WING GEOMETRY DESIGN CONSIDERATIONS FOR A NEXT GENERATION COMMERCIAL AIRCRAFT

A thesis submitted in partial fulfillment
of the requirements for the degree of
Master of Science in Aerospace Systems Engineering

by

JAY ABHILASH VORA
B.Tech. Aerospace Engineering, Indian Institute for Aeronautical Engineering
and Information Technology, Pune, India, 2013

2019
Wright State University

Wright State University
GRADUATE SCHOOL

May 3, 2019

I HEREBY RECOMMEND THAT THE THESIS PREPARED UNDER MY SUPERVISION BY Jay Abhilash Vora ENTITLED Blended Wing Design Considerations for A Next Generation Commercial Aircraft BE ACCEPTED IN PARTIAL FULFILLMENT OF THE REQUIREMENTS FOR THE DEGREE OF Master of Science in Aerospace Systems Engineering.

Dr. Mitch Wolff, Ph.D.
Thesis Director

Dr. Joseph Slater, Ph.D., P.E.
Chair, Department of Mechanical and
Materials Engineering

Committee on
Final Examination

Dr. Mitch Wolff, Ph.D.

Dr. Rory Roberts, Ph.D.

Dr. James Menart, Ph.D.

Dr. Barry Milligan, Ph.D.
Interim Dean of the Graduate School

ABSTRACT

Vora, Jay Abhilash. M.S.A.S.E, Department of Mechanical and Material Engineering, Wright State University, 2019. *Blended Wing Design Considerations for A Next Generation Commercial Aircraft.*

The current aircraft design has not changed significantly in the last few decades. Growing environmental concerns and fuel prices are driving manufacturers to develop unconventional but efficient aircraft configurations. The blended wing body (BWB) configuration provides an alternate and more efficient means of subsonic travel. The BWB aircraft replaces the traditional wings and fuselage with hybrid wing shape where the fuselage and wings have integrated. Major aircraft manufacturers are researching the BWB concept incorporating electric propulsion for civil transport use.

In this research a 300 passenger BWB aircraft aerodynamic shape is designed. This aircraft is used to assess the aerodynamic efficiency of the BWB design over a conventional tube aircraft design. The study utilizes Computational Fluid Dynamics (CFD) tools to analyze the fluid flow at different angles of attack for the BWB geometry. A conceptual BWB aircraft was designed using the parameters of a conventional aircraft configuration. During the design, the compatibility of the BWB aircraft with the current airports was also considered. The 3D Computer Aided Design (CAD) software SolidWorks was used to create the BWB design. ANSYS Fluent was used to perform the computational aerodynamic analysis. Aerodynamic flow parameters were investigated to determine the feasibility of a BWB aircraft for commercial flight.

Contents

List of Figures

List of Tables

Acknowledgment

I would take this opportunity to extend my sincerest thanks to Dr. Mitch Wolff for his support and guidance throughout the entire design and analysis process for the Blended Wing Body conceptual aircraft. He gave me an exciting opportunity to work on am original aircraft design. He continuously provided direction to the thesis, guiding me towards the conceptual design and CFD analysis for BWB aircraft. This research would not have been possible without his encouragement and support.

I would like to thank my committee members Dr. Rory Roberts and Dr. James Menart. I would also thank Mr. Charles Stevens, whose input was valuable to the project. His assistance with the ANSYS software, especially with the meshing process was essential to the project. A big thank you to Mike Vanhorn for his help and technical support with the different software and other computational resources at Wright State University.

Finally, I would like to thank my parents and my family for their unwavering love and support as I pursued my Master degree. They are my inspiration, and I work hard to make them proud.

List of Symbols

a	Acceleration
C	Chord Length
C_f	Skin Friction Coefficient
C_L	Lift Coefficient
$C_{l_{max}}$	Maximum Lift Coefficient
C_D	Drag Coefficient
$\frac{D}{Dt}$	Material Derivative
D_ω	Cross Diffusion Term
E	Energy
F	Force
F_{Lift}	Lift Force
F_{Drag}	Drag Force
g	Acceleration due to Gravity
G_k	Generation of Turbulent Kinetic Energy
G_ω	Generation of dissipation rate
k	Turbulent Kinetic Energy
K	Kelvin
LH_2	Liquid Hydrogen
M_∞	Freestream Mach number
m	Mass
p	Pressure
$p - p_\infty$	Aerodynamic Pressure Differential
U_∞	Freestream Fluid Velocity
Re	Reynolds Number
S	Surface Area
S_k, S_ω	User Defined Source Term
t	Time
u	x-component of Free Stream Velocity
u_i, u_j, u_k	Component of Free stream Velocity
u_f	Friction Velocity
V	Free Stream Velocity
v	y-component of Free Stream Velocity
w	y-component of Free Stream Velocity
Y_k, Y_ω	Dissipation of k and ω
y_1	First Cell Height
ρ	Fluid Density
μ	Dynamic Viscosity
ν	Divergence
$\frac{\partial}{\partial t}$	Partial Derivative
ω	Specific Dissipation rate
Γ_ω, γ_k	Effective Diffusivity of k and ω
τ	Wall Shear Stress
τ_{ij}	Wall Shear Stress Component

Acronyms

ACP	Advanced Concepts for Aeronautic Design
AoA	Angle of Attack
BLI	Boundary Layer Ingestion
BWB	Blended Wing Body
CAD	Computer Aided Design
CAGR	Compound Annual Growth Rate
CFD	Computational Fluid Dynamics
HWB	Hybrid Wing Body
NASA	National Aeronautics and Space Administration
NACA	National Advisory Committee for Aeronautics
PDE	Partial Differential Equation
RANS	Reynolds Averaged Navier Stokes
TeDP	Turbo-electric Distributed Propulsion
UAV	Unmanned Aerial Vehicle
USAAF	United State Army Air Force

Introduction

The Wright Flyer was first designed and flown in 1903, a first heavier than air powered aircraft. A short 30 years later Boeing introduced 247, a 10-passenger twin-engine monoplane - the first commercial aircraft. It was the first aircraft with fully cantilever wing and retractable landing gear to reduce the drag. A comparison of the two aircraft shows a remarkable engineering accomplishment within a short span of 30 years. A decade later Boeing introduced the B47. The design of B47 represents the most fundamental design characteristic of a modern subsonic aircraft: swept wing and empennage and podded engines hung beneath the wing. Boeing 787 designed almost six decades later appears to be equivalent. It suffices to say that the current design of commercial aircraft has not changed significantly in the last few decades; rather incremental performance optimization has taken place with each new generation of aircraft.

1.1 Project Overview

On a global scale, passenger air traffic is going to maintain positive growth rates up to 2030. In the next 20 years the number of airline passengers is expected to grow at a compound annual growth rate (CAGR) of 4.7 percent [22] as shown in Figure 1.1(a). In the next 20 years, it is projected that a total of 23000 new aircraft will be added into service[23] as shown in Figure 1.1(b). These aircraft will have to fulfill the demands for reduction in environmental impact and flight operating costs, particularly because of NOx limitations, noise

pollution around airports and rising fuel prices. In order to meet environmental limitations and future traffic growth, a cross disciplinary effort is required that focuses on revolutionary aircraft design, advanced propulsion system, noise reduction and efficient fuel consumption to achieve desired flight attributes.

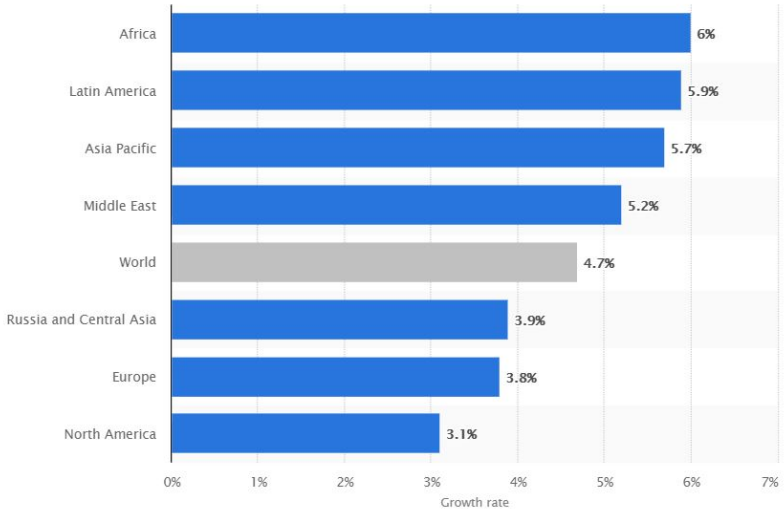

(a) Estimated compound annual growth rates for passenger air traffic from 2018 to 2037, by region[22]

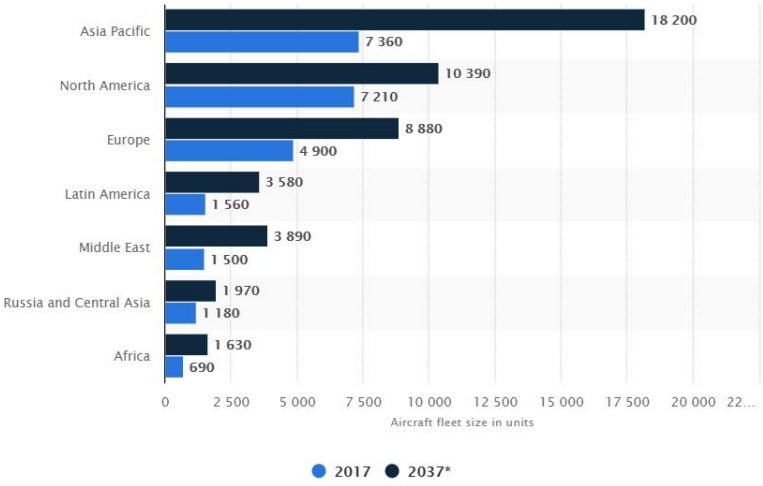

(b) Size of aircraft fleets by region worldwide in 2017 and 2037 (in units)[23]

Figure 1.1: Annual Passenger Growth and Fleet Demand over the Next 20 Years

In recent years many aircraft manufacturers and universities are researching and developing unique aircraft configuration for future air transport needs. Within these uncon-

TECHNOLOGY BENEFITS*	TECHNOLOGY GENERATIONS (Technology Readiness Level = 4-6)		
	N+1 (2015)	N+2 (2020**)	N+3 (2025)
Noise (cum margin rel. to Stage 4)	-32 dB	-42 dB	-71 dB
LTO NOx Emissions (rel. to CAEP 6)	-60%	-75%	-80%
Cruise NOx Emissions (rel. to 2005 best in class)	-55%	-70%	-80%
Aircraft Fuel/Energy Consumption‡ (rel. to 2005 best in class)	-33%	-50%	-60%

* Projected benefits once technologies are matured and implemented by industry. Benefits vary by vehicle size and mission. N+1 and N+3 values are referenced to a 737-800 with CFM56-7B engines, N+2 values are referenced to a 777-200 with GE90 engines

Figure 1.2: NASA Next-Generation Aircraft System Level Metrics[26]

ventional designs, one of the most promising aircraft design concept is the flying wing configuration. A BWB also known as a hybrid-wing body (HWB) essentially blends the wings and the fuselage resulting in a large flying wing. The BWB design is essentially a single lifting surface and thus a clean aerodynamic configuration. National Aeronautics and Space Administration's (NASA) subsonic fixed-wing project has identified four technical design parameters for future aircraft designs. These parameters are presented in Figure 1.2. The N+1 aircraft denotes the traditional tube and wing aircraft configuration. NASA has been working on the concept of BWB for several years. The N3-X represents the most recent generation of the BWB concept. It has a revolutionary propulsion concept called Turboelectric Distributed Propulsion (TeDP) that uses electricity to generate all main propulsion power thus drastically reducing the fuel requirements[18]. The BWB aircraft and the TeDP will help in achieving the N+2 and N+3 goals.

1.2 Scope

The scope of this thesis focuses on the aerodynamic analysis of a conceptual BWB aircraft. A hybrid wing body aircraft is characterized by airfoil-shaped fuselage which smoothly blends into the wing. This concept has been widely studied and researched and the results

suggest remarkable performance improvements over the conventional aircraft. The BWB configuration exploits a thick airfoil shaped fuselage in the center[15]. It accommodates the passenger cabins, cargo, and the equipment in the thick central structure, effectively reducing the aerodynamic load on the outboard wings. Since the biggest chord is located at the center, it needs low lift coefficient to bear the elliptical spanwise lift distribution[15]. It also reduces the total drag because its airfoil like central body with no tail, blends with the wings[15]. In this configuration, most trapezoidal planform area is covered by the wings thus reducing the wing area effectively reducing the skin friction drag[15].

The background of the BWB is discussed in chapter 2 which reviews the development of the aircraft configuration and future challenges. NASAs N3-X, an excellent example of BWB design is discussed. In chapter 3, the design methodology for the conceptual BWB design are discussed. Chapter 4 discusses the computational approach taken for the CFD analysis. The following two chapters discuss the results of the computational analysis and aircraft performance. It also discusses the findings, conclusion and further areas of research.

1.3 Objective

The primary objective of this research is to perform a preliminary aerodynamic analysis on the BWB aircraft. More specifically the lift and drag force analysis of an BWB design configuration. Design details like the turbogenerators, control surfaces, landing gear, are not considered for this thesis. Hence an inviscid analysis followed by some spot checks for viscous aerodynamic performance is carried out. The aircraft is designed using NASA's N3-X aircraft as a baseline. The main goal is to establish whether the configuration could be better than conventional modern aviation aircraft. The task of the thesis are:

- Develop the 3D design of a BWB aircraft using the N3-X model as the baseline

- Perform aerodynamic simulation of the designed aircraft using computational methods.
- Perform grid independent study
- Develop the pressure and velocity contours to study the flow pattern.
- Calculate the coefficient of lift and coefficient of drag. Calculate the L/D for the designed configuration

Background

BWB or HWB has been a design concept for a very long time. Some aircraft based on a blended wing body from history are discussed.

2.1 Remington - Burnelli Airliner

Pioneering aviator Vincent J, Burnelli came up with the idea of an airfoil shaped fuselage that could be used as a lifting body. In 1921, he designed an aircraft RB-1 (Figure. 1.2), a twin biplane with airfoil shaped fuselage. The gross weight of the aircraft was 14,637 lb and the normal fuel capacity of the machine was 7.5 hrs [25]. The designed wing loading was 9 lb./sq. ft. and the airfoil shaped fuselage contributed to the lift by carrying 5 lb./sq. ft.[25]

2.2 Northrop Flying-Wing

In the 1920s, John Northrop was a leading promoter of the flying-wing design aircraft in the United States[17]. In 1929 the prototype for a flying wing known as X-216H (Figure.2.2(a)) was flown. After 11 years, the N-1M 'Jeep' (Figure.2.2(b)), one of the progressions of experimental all-wing aircraft design was developed. The aircraft was first tested at Muroc Dry Lake in July of 1941[20]. In the next two years, more than 200 flights were

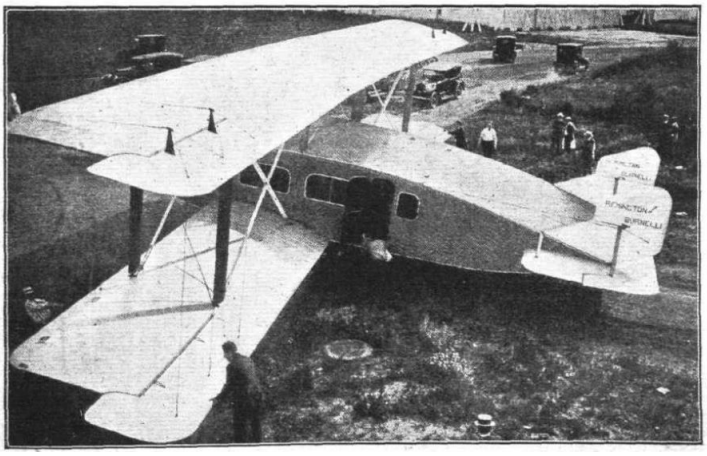

Figure 2.1: Remington-Burnelli Airliner - RB1
[25]

made to gather performance data[17]. Northrop then developed a series of large Flying-Wing bombers for the United States Army Air Force (USAAF) during the 1940s. The YB-49 (Figure. 2.2(c)) developed after World War II (WWII) was a flying wing jet-powered bomber. These two YB-49 were modified YB-35s, replacing four radial engines with eight turbojet engines. The aircraft had four vertical stabilizers; two on each wing and four air dams to minimize span-wise flow. Flight testing showed good performance; however, stability issues during the flight testing ensured that they never entered production[21][27]. The design work and the experimental data gathered during the testing laid the foundation for the development of the B-2 stealth bomber nearly after 40 years. The B-2 'Spirit' stealth bomber was developed in 1989 by Northrop Grumman. The bomber had a sophisticated modern control system and can cover long ranges. (Figure. 2.2(d))

2.3 The Horten Brothers - All Wing Aircraft

The Horten Brothers, Reimar and Walter were German aircraft homebuilders. The treaty of Versailles limited the construction of German military airplane, this led to an increase in glider flying and soaring in Germany[13]. As teenagers, the Horten brothers became

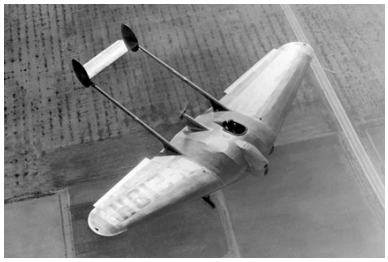

(a) Northrop Flying Wing X-216H[7]

(b) Northrop N1-M 'Jeep"[17]

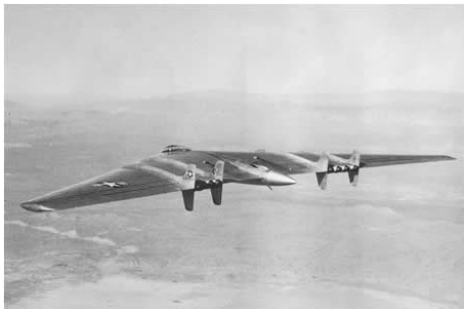

(c) Northrop YB-49[27]

(d) Northrop B-2 'Spirit' Bomber[3]

Figure 2.2: Northrop Flying Wing Family

involved in glider design and flying. During WWII, the Horten brothers designed all-wing aircraft with continually improving performance. The first glider Horten Ho I (Figure. 2.3(a)), was first tested in July 1933[13]. Although it was not a complete success, it opened way the for more flying wing models including the Ho IV [13](Figure. 2.3(b)). In 1944, Horten Ho IX with turbojet engines made its first flight. It was a big success. As the war ended, Horten brothers emigrated to Argentina where they continued to develop their flying wing[13].

2.4 Armstrong Whitworth AW.52

Britain joined the Americans and Germans in the pursuit of a flying wing aircraft with their Armstrong Whitworth AW.52 prototype (Figure. 2.4). It was a tailless configuration with

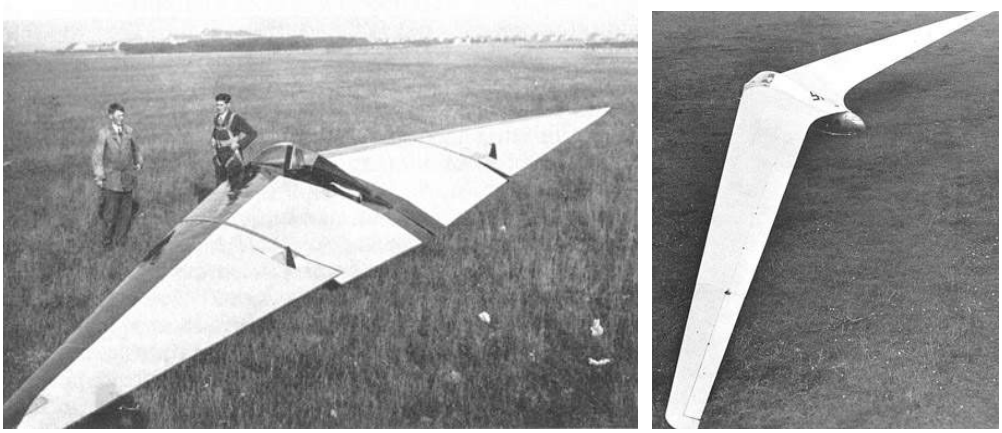

(a) Horten Ho I[13] (b) Horten Ho IV"[13]

Figure 2.3: Horten Brothers Flying Wing Gliders

pure jet propulsion, 35° wing sweep-back and had vertical surfaces at each wing tip for yaw control[24]. The aircraft first flew in 1947; however, it never entered production[24].

Figure 2.4: Armstrong Whitworth AW. 52
[6]

2.5 BWB design of NASA and Boeing Co.

In 1988, Dennis M. Bushnell, senior scientist of NASAs Langley Research Center addressed a gathering of innovative leaders with a question: is there a renaissance for the

long-haul transport?[14]. His perspective was that the development in aerodynamic performance for commercial transports had declined wherein incremental benefits were becoming smaller and smaller [14]. Robert H. Liebeck of McDonnell Douglas Corporation (now The Boeing Company) simulated by his discussion with Bushnell, along with his associates conducted a clean piece of paper [14] brief study and arrived at a BWB configuration (Figure 2.5). This started the collaboration between Boeing and NASA for the development of the BWB commercial aircraft. In 1994, NASA initiated the research and development of a BWB aircraft under a new program Advanced Concepts for Aeronautics Program (ACP)[14]. It was composed of the McDonnell Douglas team, NASA team and various universities around America. One of the important highlights of the ACP studies was the successful testing of a scaled, remotely controlled model of the BWB configuration. The NASA ACP sponsored studies ended in 1998. It was concluded that the performance of the BWB configuration over the convention aircraft in terms of L/D, reduced fuel burn and reduction in direct operating cost was revolutionary. The research continued in the early 2000s with Boeing starting construction of an unmanned 14% scaled BWB transport. The project was named X-48.

The Boeing X-48 series was an experimental, scaled Unmanned Aerial Vehicle (UAV) specifically designed to research the characteristics of the BWB aircraft. The Boeing X-48A was a 10.7m (35ft) span aircraft but the project was canceled in 2004[5]. Research then focused on a new model, the X-48B (Figure. 2.6(a)). It had a wingspan of 6.4m (21ft) and was built with composites. It was powered by three small turbojet engines. Testing on the X-48B began in 2007 at the Dryden Flight Research Center in California. During the initial test, low speed and low altitude characteristics were studied including stall and handling characteristic[5][4]. In phase II, high-speed flight test and controllability were investigated[5]. A modified version of the X-48B called the X-48C (Figure. 2.6(b)) was introduced later in 2012. It was a two-engine configuration with a wingspan of 6.4m. The aircraft had upgraded flight control systems, an airframe-noise shielding configuration,

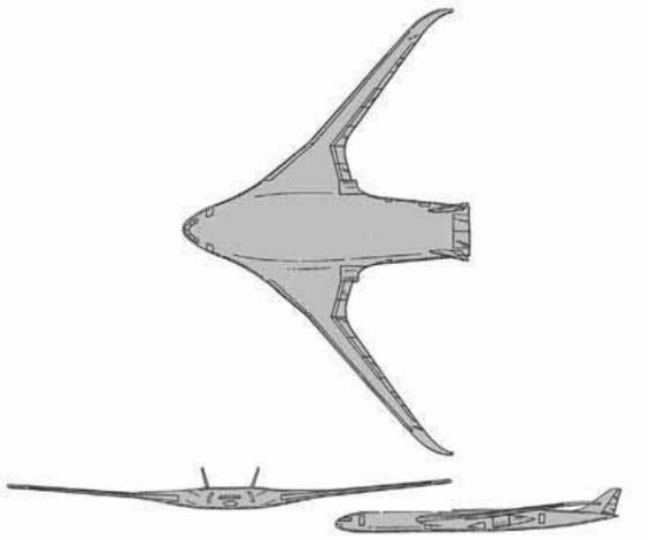

Figure 2.5: BWB Configuration by McDonnell Douglas Company
[14]

vertical fins and flight control limiters[5]. The main objective of the X-48C was to test the superior controllability and low-noise capability[4]

(a) Boeing X-48B[4] (b) Boing X-48C[4]

Figure 2.6: Boeing X- Series UAV

2.6 NASA Electric Propulsion HWB: N-3X

NASA N3-X is the most ambitious BWB design concepts. It integrates the flying wing concept with an innovative propulsion concept to reduce the fuel burn as well as noise

emissions. The thrust for the N3-X (Figure. 2.7) is provided by an array of 14 motor-driven electric fans mounted on the top of the fuselage at the aft[18]. The electric power to operate the fans is provided by wing-tip mounted turboshaft mounted engines. The aft fans will also help with the boundary layer ingestion thus reducing the drag.

Figure 2.7: NASA N3-X Aircraft
[1]

The design specification for the N3-X is provided in Table. 2.1

Table 2.1: NASA N3-X Basic Design Specification

WingSpan	64.91 m^2
Wing/Fuselage Gross Area	860 m^2
Aspect Ratio	4.9 m
Overall Length	41 m
Max take-off Mass	225,022 Kg
Max Range	8,680 nm
Mach Limit	0.89

Blended Wing Body Design

The N3-X was proposed as a 300-passenger aircraft employing a TeDP system. Two large turbogenerators were placed at the wing tips to feed the engines with uniform free stream velocity. The propulsors - array of fans are distributed on the upper surface of the fuselage near the trailing edge of the BWB in a mail-slot inlet nozzle[9][10]. The 3D model for the NASA N3-X was not provided. The conceptual model was created using the basic dimensions of the N3-X and other known parameters for a BWB design. The design of the BWB aircraft is strictly based on NASAs N3-X configuration.

3.1 Airfoil Selection

The design was divided into two parts the fuselage and the outer wing. The total span of the aircraft was 64.908 m, and the total length was 41.0 m. The dimensions for the model were obtained from the Cranfield N3-X drawings and reports[18]. The reports did not provide any details on the airfoil used for the wing and the fuselage section. A preliminary study was performed for suitable airfoil design for the fuselage and the wing design.

For a BWB design, the fuselage is airfoil shape and hence needs to be sufficiently thick to hold 300 passengers and their cargo. For BWB configuration the fuselage is divided into three sections: forward fuselage, center fuselage, and aft fuselage(Figure: 3.1). The cross-section shape of the BWB fuselage changes dramatically from forward to aft. The forward fuselage mainly houses the pilot cabin and the nose landing gear. The center

fuselage houses most of the passengers and the cargo. The forward and center fuselage is the pressurized section of the fuselage. The aft fuselage, on the other hand, is not pressurized and houses many essential components of the aircraft like cooling systems (LH_2 tanks or the cryocooler)[18], batteries and multiple piping routes for the electric fans. The wing as in a conventional aircraft houses the fuel tanks. It also houses electrical cables and cooling pipes for electricity transfer from the turboshaft engines to the fan array.

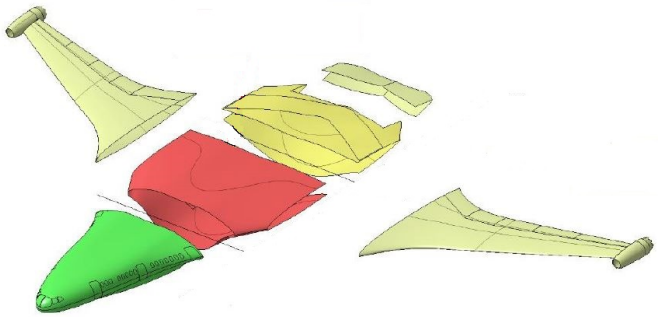

Figure 3.1: Divison of Fuselage for BWB Aircraft
[18]

The criteria for the airfoil selection for fuselage and wing are:

- High L/D
- Positive pitching moment
- Medium airfoil thickness

The moment coefficient plays a significant role in the longitudinal stability of the BWB aircraft. In a conventional aircraft, the cambered airfoil provides negative moment coefficient which is compensated using the horizontal tail[12]. A BWB configuration obviously cant counter-attack the negative pitching moment. Longitudinal stability of a tailless aircraft is achieved using reflex airfoils or by using sweep and twist of the wings[12]. Several airfoils were analyzed, but only the reflex airfoils were taken into consideration because of their higher longitudinal stability. For fuselage and the wing, the following

six airfoils were shortlisted: NACA 23012, NACA 25112, Eppler 635, FX 60-126, NASA SC(2)-0606, and MH-62. DesignFOIL software was used to analyze these airfoils. The results are listed in Table: 3.1.

Table 3.1: Comparison of Different Airfoil Data for Fuselage and Outboard Wing

Airfoil	$C_{l_{max}}$	$(L/D)_{max}$	**Angle of Attack for** $(L/D)_{max}$
NACA 25112	1.5413	98.11	7.25
Eppler 635	1.4023	113.43	9
FX 60-126	1.7396	112.33	4.5
NACA 23012	1.5413	96.79	8.75
NASA SC(2)-0606	1.3761	103.65	5.1
MH-62	1.2614	94.64	5.5

The goal was to select an airfoil which provides maximum lift coefficient to ensure center body acts as the main lift generating portion[12]. From Table: 3.1. NACA 23012 was the best airfoil configuration to be used for the center body. The graphs showing variation in coefficient of lift (C_l), and L/D vs Angle of Attack (AoA) for the NACA 23012 are presented in Figure: 3.2(a) and Figure: 3.2(b). The outboard airfoil should have a good lift to drag ratio, delay the onset of wave drag and good stall characteristics. NASA SC(2)-0606 was selected for outboard and tip wing sections. The graphs showing variation in coefficient of lift (C_l), and L/D vs AoA for the NASA SC(2)-0606 are presented in Figure: 3.3(a) and Figure: 3.3(b).

3.2 Conceptual 3D Model

The 3D modeling for the conceptual aircraft was done using SolidWorks 2018. The planform boundary was created using the dimensions from the NASA N3-X (Figure: 3.4(a)). The airfoil geometry was imported using the curve function in the software. The first part

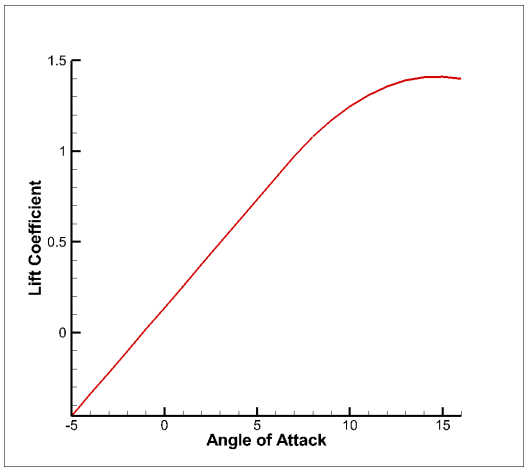

(a) Coefficient of Lift vs AoA - NACA 23012

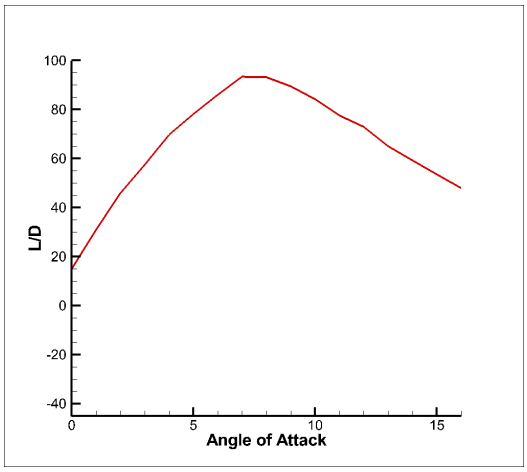

(b) L/D vs AoA - NACA 23012

Figure 3.2: Polar Plots for NACA 23012

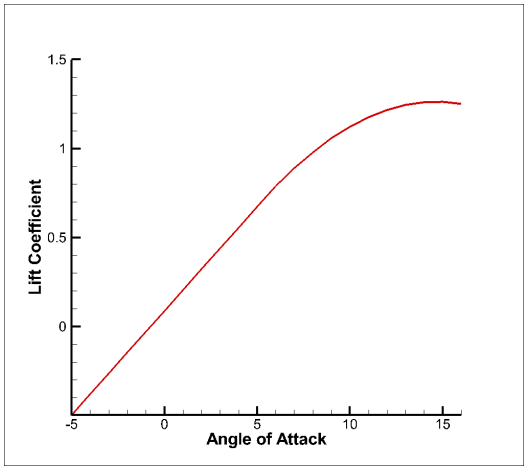

(a) Coefficient of Lift vs AoA - NASA SC(2)-0606

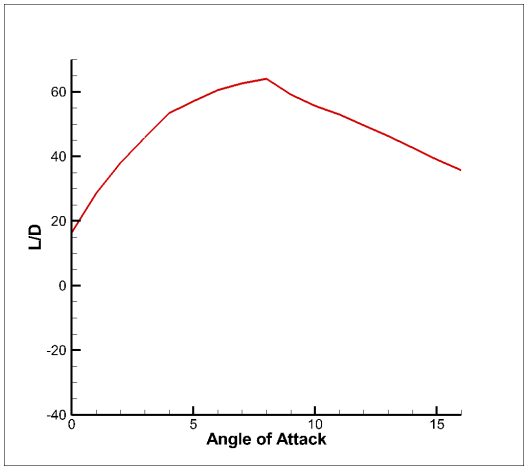

(b) L/D vs AoA - NAS A SC(2)-0606

Figure 3.3: Polar Plots for NASA SC(2)-0606

modeled was the outer wing (Figure: 3.4(b)).The model was created using sections and the ”surface loft” feature of the SolidWorks software. Since the aircraft is symmetric only half the aircraft was modeled. The ”mirror” feature was used to create the full geometry of the aircraft.(Figure:3.5).

(a) Planform View for BWB Aircraft (b) Outer Wing for BWB Aircraft

Figure 3.4: 2D Views for the BWB Aircraft

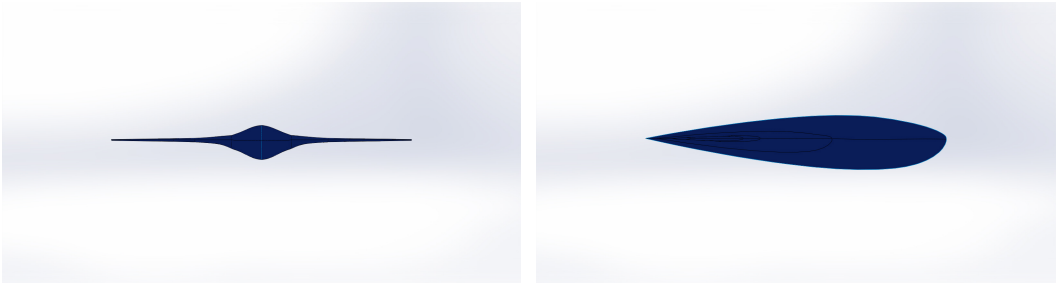

(a) Front View (b) Side View

(c) Top View (d) Isometric View

Figure 3.5: 3D Views for the BWB Aircraft

3.3 Control Volume

The use of control volumes are important for the fluent analysis. The computational domain was modeled using SolidWorks. A rectangular shaped domain measuring 85 m x 72 m x 30 m was created. The aircraft model and the domain were brought together using the ”assembly” feature. The assembly feature results in two separate solid models(Figure: 3.6). Hence the ”cavity” feature in SolidWorks was used to create a single solid geometry (Figure: 3.7). Due to the boundary conditions being used(See Section 4.4) the domain need

not be large thus saving on the computation time.

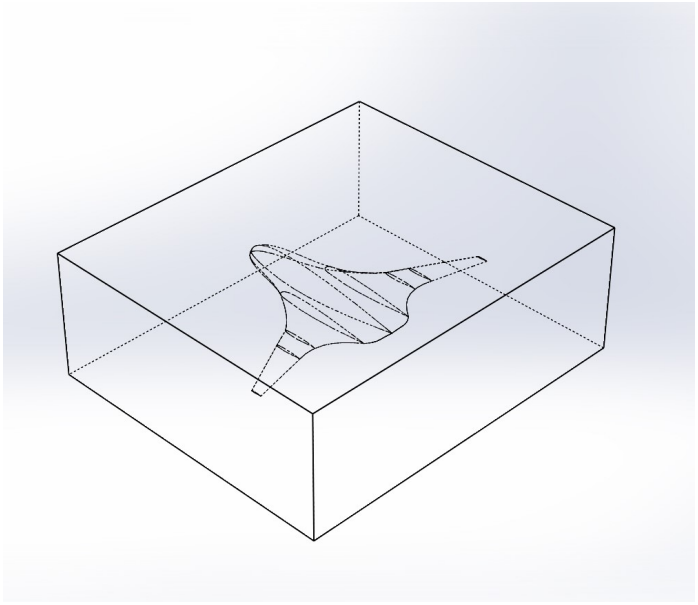

Figure 3.6: CFD Domain

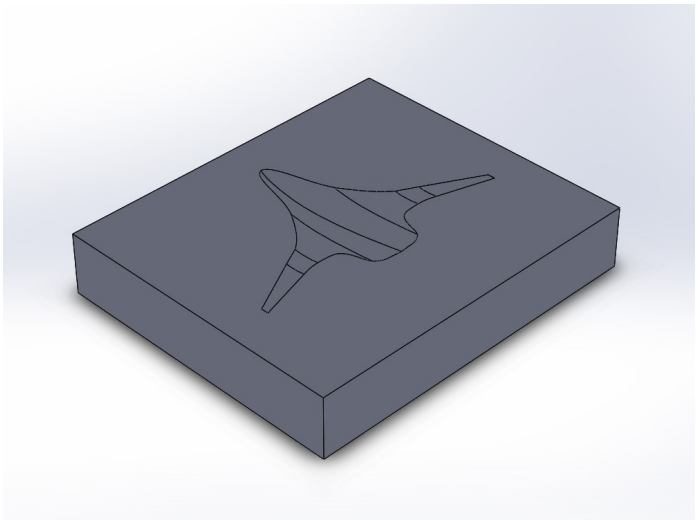

Figure 3.7: Sectional View for CFD Domain

Computational Fluid Dynamics

Simulation and Validation

After the 3D model was created, the geometry was imported into the ANSYS Workbench software for meshing and CFD simulation. For CFD simulation, ANSYS Fluent model was used for obtaining the numerical results. The model was first imported into the DesignModeler. A half model of the aircraft was utilized for CFD simulation to save on the computation time and file size. A mesh or grid was then created around the geometry to serve as locations at which to solve the flow equations. The mesh would be fine near the geometry and in any other regions where there are large flow gradients. The mesh can be coarse at a location far from the primary geometry. This helps in saving computation time. The mesh quality near the wall is a critical parameter to study the viscous effects near the aircraft wall. Once the mesh is complete, the meshed geometry is moved to the ANSYS Fluent solver. Each step of the simulation set-up is explained in detail further in the thesis.

4.1 Basic Fluid Physics

In this section, the essential fluid dynamics equations such as aerodynamic forces, Reynolds number, RANS equations and other equations used in the thesis are stated.

4.1.1 Reynolds Number

Reynolds number is a dimensionless quantity that expresses the fluid behaviour. It is the ratio of inertial forces to viscous forces[16]. It helps in predicting if the flow is laminar or turbulent. The Reynolds number is calculated using Equation. 4.1

$$Re = \frac{\rho V C}{\mu} \tag{4.1}$$

4.1.2 Lift and Drag Coefficient

The lift coefficient is a dimensionless coefficient that represents the lift force. It relates the lift generated to the dynamic pressure around the body[16]. Lift always acts perpendicular to the fluid flow direction. The lift coefficient is given by Equation. 4.2

$$C_L = \frac{F_{Lift}}{\frac{1}{2}\rho V^2 S} \tag{4.2}$$

The drag coefficient is also a dimensionless number which helps in representing the drag generated by the body[16]. The drag coefficient is given by Equation. 4.3

$$C_D = \frac{F_{Drag}}{\frac{1}{2}\rho V^2 S} \tag{4.3}$$

4.1.3 Navier-Stokes Equations

Navie-Stokes equations are use to mathematically examine the changes in a fluid flow. The Navier-Stokes are non-linear partial differential equation (PDE) that describe the motion of a viscous fluid. The equations are difficult to solve analytically and require an iterative process to solve them. The governing equations based on the conservation laws build the mathematical model for the fluid state. These equations along with the turbulence model help in solving the CFD problem. The governing equations consist of the following

conservation equations:

- **Conservation of Mass**: The equation for unsteady, 3-dimensional compressible flow is given by

$$\frac{\partial \rho}{\partial t} + \frac{\partial [\rho u_i]}{\partial x_i} = 0 \tag{4.4}$$

For a steady case, the first term will disappear and density is constant for incompressible fluid.

- **Conservation of Momentum**: The momentum equation is based on the Newton's second law of motion (mass time acceleration = force, or rate of change of momentum = force). For 3D flow the equation for conservation of momentum is given by:

$$\frac{\partial (\rho u_i)}{\partial t} + \frac{\partial \left(\rho u_j u_i\right)}{\partial x_j} = \rho g_i + \frac{\partial \tau_{ij}}{\partial x_j} - \frac{\partial p}{\partial x_i} \tag{4.5}$$

$$\frac{\partial (\rho u_i)}{\partial t} + \frac{\partial \left(\rho u_j u_i\right)}{\partial x_j} = \rho g_i - \frac{\partial p}{\partial x_i} + \mu \frac{\partial^2 u_i}{\partial x_j \partial x_j} \tag{4.6}$$

For flow in X-direction, Equation. 4.6 can be represented as Equation: 4.7

$$\rho \left(\frac{\partial u}{\partial t} + u\frac{\partial u}{\partial x} + v\frac{\partial u}{\partial x} + w\frac{\partial u}{\partial x} \right) = \rho g - \frac{\partial p}{\partial x} + \mu \left(\frac{\partial^2 u}{\partial x^2} + \frac{\partial^2 u}{\partial y^2} + \frac{\partial^2 u}{\partial z^2} \right) \tag{4.7}$$

Navier-Stokes equation can similarly be written for flow in Y-direction and Z-direction.

- **Conversation of Energy**: The equation for conservation of energy is derived using the first law of thermodynamics. It states that 'rate of change of energy is equal to the work done by the fluid and the rate of heat transferred to the fluid due to conduction'[16].

$$\frac{\partial(\rho E)}{\partial t} + \frac{\partial(\rho u_j E)}{\partial x_j} = \frac{\partial}{\partial x_j}\left(k\frac{\partial T}{\partial x_j}\right) + \frac{\partial}{\partial x_j}(\tau_{ij} v_i) \tag{4.8}$$

The momentum equation can be converted to Reynolds-Averaged equation for turbulent flow. Reynolds-Averaged equation are time averaged. The variables in the momentum equation get separated into mean (time-averaged or ensemble averaged) and fluctuating components. For velocity, the components are denoted by $u_i = \overline{u_i} + u_i'$. Hence the Reynolds-Averaged momentum equation is given by [11]

$$\frac{\partial \rho\overline{u_i}}{\partial t} + \frac{\partial}{\partial x_j}(\rho\overline{u_i u_j}) = \mu\frac{\partial^2 \overline{u_i}}{\partial x_j \partial x_j} - \frac{\partial \overline{p}}{\partial x_i} - \frac{\partial}{\partial x_j}\left(\rho\overline{u_i' u_j'}\right) \tag{4.9}$$

The term $-\rho\overline{u_i' u_j'}$ is called the Reynolds stress tensor and incorporates the effects of turbulent motion. The reynolds stress tensor is symmetric [11] and must be modeled to solve Equation: 4.9.

4.1.4 Inviscid Model

Inviscid flow is fluid flow, in which the viscosity is zero. There are very few real-life inviscid fluid examples. However, the inviscid flow has many fluid dynamics applications. When viscous forces are neglected, the momentum equation can be simplified further to Euler Equation. For inviscid flow, $\mu = 0$, hence the momentum (Equation. 4.6) can be written as:

$$\frac{\partial(\rho u_i)}{\partial t} + \frac{\partial(\rho u_j u_i)}{\partial x_j} = \rho g_i - \frac{\partial p}{\partial x_i} \tag{4.10}$$

Euler equations are hyperbolic equation governing adiabatic and inviscid flow. Under many flight conditions, the effects of viscosity are minimal and can be ignored. Inviscid flow model requires a relatively low computational time, and cost and hence are extensively used in aerodynamic design applications.

4.1.5 Turbulence Model

The flow at certain regions will turn turbulent at higher values of Reynolds number. For a flat plate, the Reynolds number above which the flow is considered to be fully turbulent is $Re > 5 * 10^5$. It is an appropriate assumption that the flow will be turbulent for BWB analysis. In CFD analysis, variety of turbulence model available ranging from single-equation to more complex models with multiple equations. Several issues need to be considered before choosing the turbulent model.

For this study, the Shear Stress Transport (SST) $k-\omega$ model was used. The $k-\omega$ SST model is a robust turbulence model developed by Menter [19]. The $k-\omega$ SST model is an advance version of the original $k-\omega$ turbulence model. The SST formulation combines the best of the two models - robust and accurate formulation of the $k-\omega$ model in the inner parts of the boundary layer and the free stream independence of the $k-\epsilon$ model in the far field[8]. The standard $k-\omega$ model and the $k-\epsilon$ model are both multiplied by a blending function and added together. The blending function is designed in a way that activates the standard $k-\omega$ model near the wall region and $k-\epsilon$ model while moving away from the surface. The SST model incorporates a damped cross-diffusion derivative term in the ω equation[8]. The $k-\omega$ SST model also has good behavior in adverse pressure gradients and separating flow[8]. The $k-\omega$ SST model introduces two equations:

$$\frac{\partial}{\partial t}(\rho k) + \frac{\partial}{\partial x_i}(\rho k u_i) = \frac{\partial}{\partial x_j}\left(\Gamma_k \frac{\partial k}{\partial x_j}\right) + G_k - Y_k + S_k \tag{4.11}$$

$$\frac{\partial}{\partial t}(\rho \omega) + \frac{\partial}{\partial x_i}(\rho \omega u_i) = \frac{\partial}{\partial x_j}\left(\Gamma_\omega \frac{\partial \omega}{\partial x_j}\right) + G_{\omega k} - Y_{\omega k} + S_\omega + D_\omega \tag{4.12}$$

The above equations model the transportation equations for turbulent kinetic energy (k) (Equation: 4.11) and the specific dissipation rate (ω) (Equation: 4.12).

4.2 Computational Fluid Dynamic Model Setup

CFD is the a numerical solution of flow based on governing equations, and flow properties explained in Section: 4.1. CFD analysis consists of three steps:

- Pre-processor
- Solver
- Post-Processor

The pre-processor deals with the input of the 3D model and mesh generation. The solver sets up the governing equations, the boundary conditions, and solver models. The post-processor help in visualization, force calculation, particle tracking. ANSYS Fluent 19.1 software is used to perform the CFD analysis on the designed BWB aircraft. ANSYS Fluent workbench is used to set up each iteration for the simulation.

4.2.1 Pre-Processor

The pre-processor converts the user-input into a mathematical problem for the solver. There are various stages involved in the pre-processing. In ANSYS Fluent pre-processing is divided into two parts: geometry import and meshing.

There are two options available in ANSYS for geometry import and modifications, DesignModeler or SpaceClaim. SpaceClaim is the latest software from ANSYS offering wide range modeling options. However, the 3D model was already created with the domain and geometry, and therefore, Design Modeler was used to import the geometry in Parasolid `(.x_t)` file format. In DesignModeler, the full model was imported(Figure: 4.1). A symmetric plane was defined, so the geometry is split into half(Figure: 4.2) for mesh generation and further calculations. The geometry can also be split in SolidWorks and then

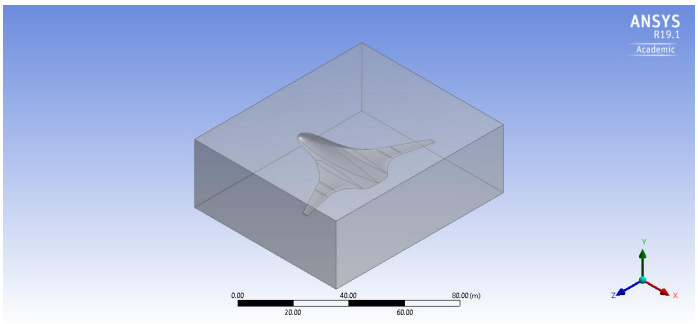

Figure 4.1: Geometry Import in DesignModeler

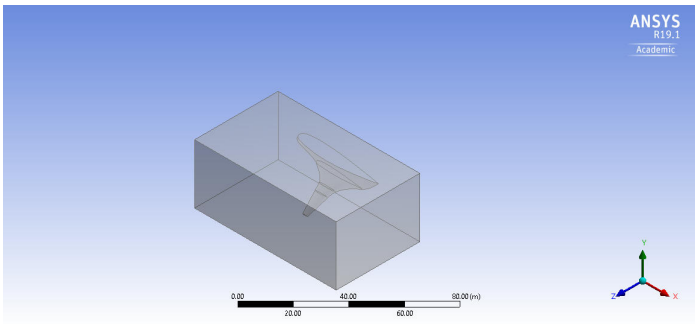

Figure 4.2: Geometry After Symmetry Plane

imported in the DesignModeler. However, defining the symmetry plane in DesignModeler is convenient since it is defined for the entire setup.

4.2.2 Meshing

Meshing is merely dividing the control volume into smaller non-overlapping domains called cells or elements. It is a very critical part of flow simulation. A carefully crafted mesh influences the accuracy of the simulation. Before the final analysis, several mesh models were created for the simulation. The mesh is created using ANSYS Meshing. ANSYS ICEM can also be used to generate a mesh. ICEM is primarily used to create a structured mesh. A structured mesh is an oriented mesh and therefore suitable for a simple geometry. For a complex geometry like the BWB, a structured mesh will lead to a lot of differently oriented meshes that need to be manually structured which will be very time-consuming. Hence for the BWB aircraft, an unstructured tetra mesh was used to divide

the volume. The tetra element is universal and is easy to use with complex geometry with minimum user input.

Mesh for Inviscid Flow Analysis

The mesh was created using the minimum mesh size of 0.9 m. The mesh was set to capture curvature and proximity. Curvature feature was used to ensure that more elements are generated near the curved surfaces and proximity feature ensures fine grid near narrow geometry. The growth rate was reduced to 1.05 to ensure that the mesh transition from coarse to fine mesh is smooth. During mesh generation, body sizing was used to refine the mesh on the aircraft body and near the aircraft geometry. A total of 19.5 million elements were created using this method(Figure: 4.4) . A grid refinement study is of vital importance to show that the numerical results are independent of the grid (i.e., the finer mesh yields the same result). A coarse mesh was created using the body sizing with a minimum element size of 1.5 m. The growth rate and other criteria were kept the same. The total number of element for a coarse mesh was 16.9 million elements(Figure: 4.3). For a fine mesh the body sizing with a minimum element size of 0.6 m. The growth rate was kept the same as in the coarse and the medium mesh. The total elements in the fine mesh were 22.4 million (Figure: 4.5). The above geometry was used to perform the inviscid flow simulation. Hence no boundary layer meshing was performed.

Mesh for Viscous Flow Analysis

For viscous flow analysis using the $k - \omega$ SST turbulence model is used. The boundary layer is defined as the thin region near the surface on the body in which viscous effects are important. The boundary layer is very thin, and the gradients of the flow across the layer are much greater. Hence very fine elements need to be created near the aircraft body. To

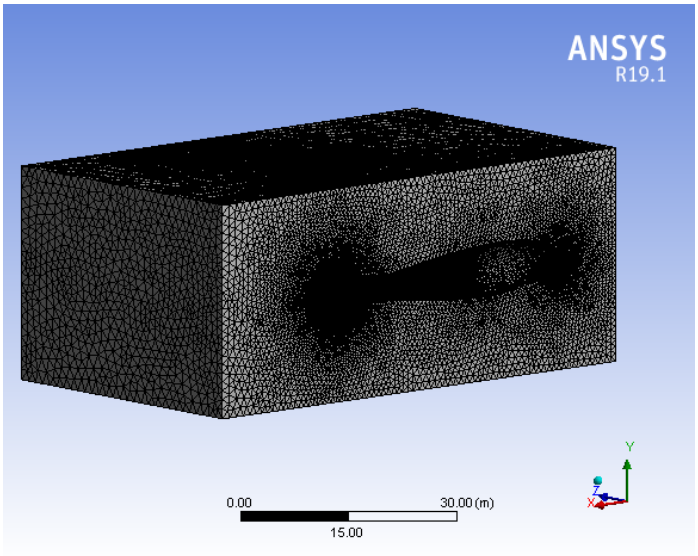

Figure 4.3: Coarse Mesh Geometry

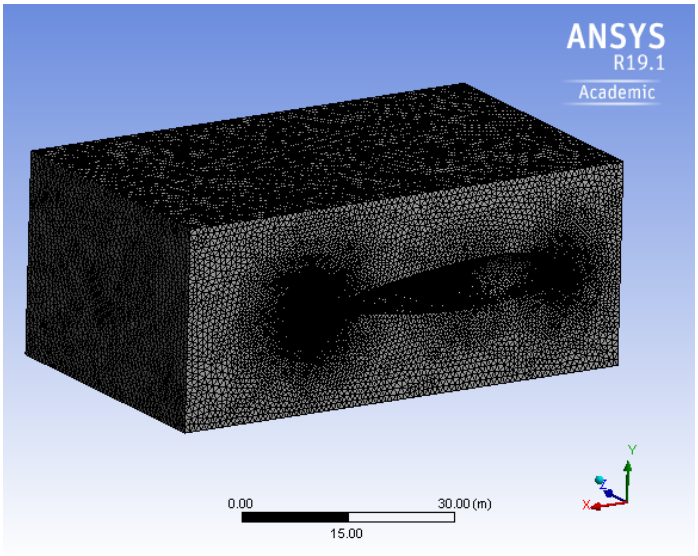

Figure 4.4: Medium Mesh Geometry

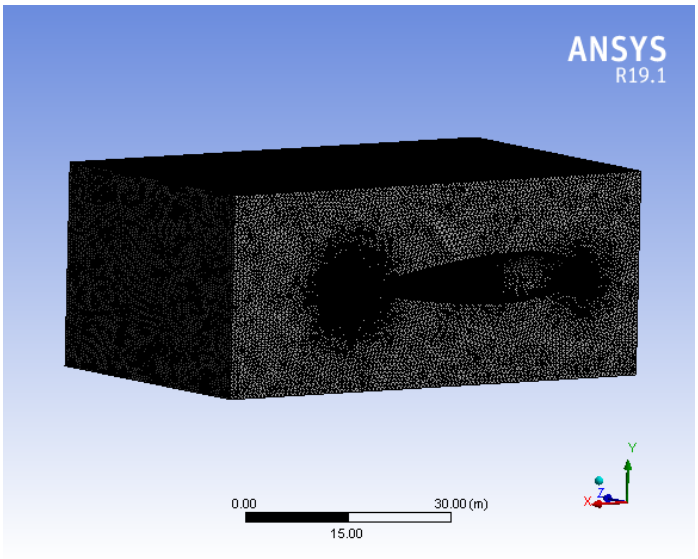

Figure 4.5: Fine Mesh Geometry

distinguish different regions of the boundary layer the concept of wall y^+ has been introduced. y^+ is a dimensionless quantity described as the distance from the surface measured in terms of viscous lengths. ANSYS Inflation is used to generate the layers near the aircraft body. Inflation creates a boundary layer of brick elements around the aircraft. The thickness of the boundary layer is calculated using the y^+ value. Based on the y^+ value the first cell height is calculated. 4.13

$$y^+ = \frac{\rho u_f \Delta y_1}{\mu} \tag{4.13}$$

where u_f is the friction velocity and y_1 is the first cell height. The friction velocity is calculated using Equation. 4.14.

$$u_f = \sqrt{\frac{\tau}{\rho}} \tag{4.14}$$

The wall shear stress τ can be calculated using Equation. 4.15

$$\tau = \frac{1}{2} C_f \rho V^2 \tag{4.15}$$

Here C_f is the skin friction coefficient and can be estimated using Equation:4.16. It is an empirical based estimation.

$$C_f = 0.058Re^{-0.2} \tag{4.16}$$

For the majority of high-Reynolds-number flows, the wall function approach is suitable. The wall function approach is reasonably accurate and converges faster. The $k-\omega$ SST turbulence model requires the y^+ to be less than 300 for wall function approach. However, to capture the low-Reynolds number effect near the surface desired y^+ value should be less than 1. Hence more layers are needed to ensure that get y^+ value around 1. For $k-\omega$ SST turbulence model analysis, the first layer height was set to 0.001 m, and the total number of layers was set to 40(Figure: 4.6).

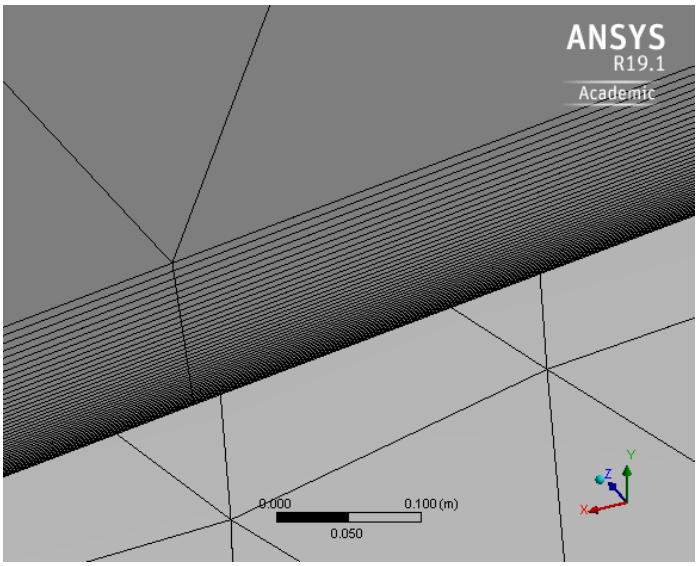

Figure 4.6: Boundary Layer Mesh

The minimum element size for the viscous flow analysis was set to 1.5 m and the body sizing minimum element size was set to 1.5 m. The growth rate was set to 1.05 as in previous mesh geometry. The total of number of 21.8 Million elements were generated for the $k-\omega$ SST turbulence model. The details for each mesh geometry is listed in Table.

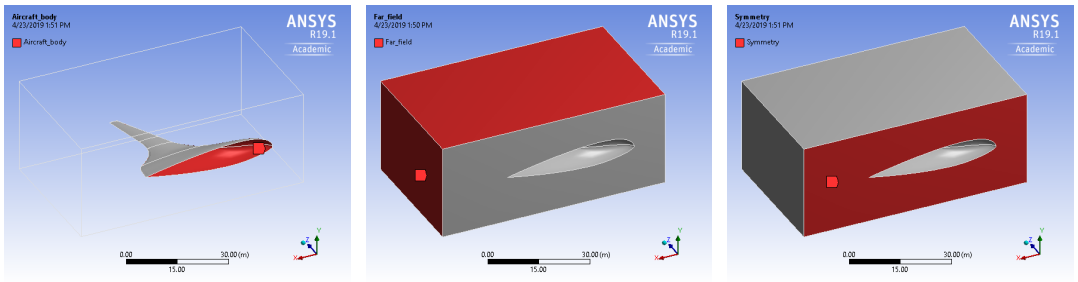

(a) Named Selection - Aircraft Body (b) Named Selection - Far Field (c) Named Selection - Symmetric Plane

Figure 4.7: Named Selection for Mesh Geometry

4.1.

Table 4.1: Mesh Specification for Inviscid Flow Model

Mesh	**No. of Elements**	**Min. Element Size**(m)	**Min. Body Element Size**(m)	**Growth rate**
Coarse Mesh	16,973,529	1.5	1.5	1.05
Medium Mesh	19,583,736	0.9	0.9	1.05
Fine Mesh	22,365,997	0.7	0.6	1.05
Viscous Flow Mesh	21,895,934	1.5	1.5	1.05

Another important task in meshing is the naming of the boundary zones. This helps in setting up the conditions in the solver of ANSYS. For all four geometry, the named selection was the same. The aircraft surface was named as aircraft body, the symmetric plane was named symmetry and all other surfaces were named as far-field(Figure: 4.7). Figure. (4.8) shows some important views of the mesh.

4.3 Numerical Setup

ANSYS Fluent has two types of solvers - pressure based solvers and density based solvers. The density-based solver is mainly used for simulating supersonic flows. For BWB simula-

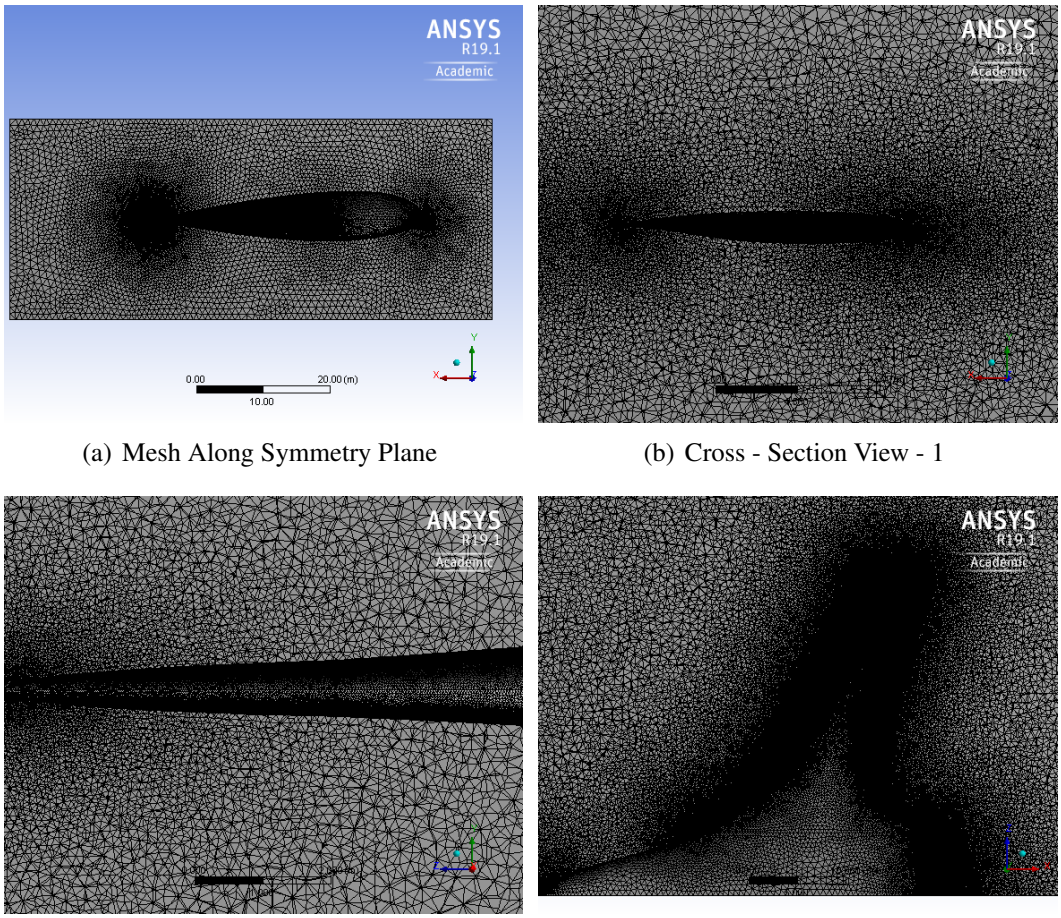

(a) Mesh Along Symmetry Plane

(b) Cross - Section View - 1

(c) Cross - Section View - 2

(d) Cross - Section View - 3

Figure 4.8: Detail Mesh Images for Medium Mesh

tion, pressure based solver was used. For the pressure based solver, the governing equations are nonlinear and coupled to one another and hence are solved using an iteration process. There are two pressure based algorithms available in Fluent - segregated and coupled. In the segregated algorithm, the governing equations are solved sequentially i.e., pressure equation is solved first and then the momentum equation. The pressure based coupled algorithm solves the coupled system of equations[2]. Since the governing equations are resolved simultaneously, the solution converges faster compared to the segregated algorithm. On the downside, the memory requirements increase by 1.5-2 times[2]. For the BWB simulation, pressure based coupled solver with second-order upwind discretization was used. The upwind discretization scheme is very stable even on a coarse mesh. The simulation was

obtained using two separate flow models: inviscid flow, and $k - \omega$ SST turbulence model.

4.4 Boundary Conditions

The flow domain needs to have boundary conditions to define the flow problem and solve the system of equations. ANSYS Fluent offers a variety of predefined boundary conditions. Based on the numerical simulation performed, correct boundary conditions need to be defined at the boundaries. The named selections defined in section 4.2.2 and shown in Figure: 4.7 was used to define the boundary conditions.

- **Aircraft Body**

  $Wall$: Used to define the solid wall boundary with no-slip condition. The roughness height and roughness constant are set to their default value.

- **Far Field**

  $PressureFarField$: Pressure far field conditions are used define the free-stream condition at infinity. We define the free stream Mach number and static conditions used for the flow simulation. The static conditions used are at altitude of 35000 ft. Hence the pressure is 23911.01 Pa, Mach number is 0.75, and the temperature is 219.477 K. The free stream velocity angle is also defined in this section. Using the pressure far field conditions activates the ideal gas equation. Hence density and other parameters are calculated using the ideal gas equation.

- **Symmetry**

  $Symmetry$: Symmetry condition is used to define the symmetric plane. This helps in reducing the computational time and cost.

The case was run for different angles of attack AoA = 0°, 3°, 5°, 8°, 9°, 10°, 11°, 12°, and 15° for inviscid flow and AoA = 0°, 3°, and 5° for viscous flow. For the grid refinement

study the simulation was performed at 3° angle of attack and atmospheric condition of 35000 ft. All the cases were hybrid initialize.

Results

The primary function behind the modeling and simulation of the BWB aircraft is to determine the lift and drag coefficient and calculate the lift to drag ratio for the conceptual BWB aircraft. The results are presented in three stages. First, the grid refinement study was performed for inviscid flow analysis to ensure that the results obtained are not grid dependent. Once the optimum mesh was determined analysis was performed for the various angles of attack at 35000 ft altitude conditions. In the final stage, mesh with boundary layer was utilized to perform viscous flow analysis using the $k-\omega$ SST turbulence model. The accuracy of the simulation was calculated by tracking the residuals for the governing equations ensuring they converged. ANSYS default converging criteria was used. The stability of the relevant integrated quantities is also considered to determine the solution convergence.

5.1 Grid Refinement Study

For the grid refinement study the coasre mesh, medium mesh and fine mesh were utilized. The details for the each mesh are provided in Section. 4.2.2, Table, 4.1 and Figure. 4.3, Figure. 4.4 and Figure. 4.5. The change in lift and drag forces are considered for the study. The results of the mesh independence study are presented in Table. 5.1

There is no considerable difference between the lift and drag force values for all three mesh size. However, the change is almost insignificant for the medium and the fine mesh.

Table 5.1: Grid Independent Study

Mesh	**No. of Elements**	**Lift Force** (N)	**Change**	**Drag Force** (N)	**Change**
Coarse Mesh	16,973,529	1929036	0.381%	119351	0.131%
Medium Mesh	19,583,736	1922849	0.059%	119211	0.014%
Fine Mesh	22,365,997	1921704		119194	

The minimum orthogonal quality for the medium mesh was 0.23, compared to 0.15 of the coarse mesh. For a good quality mesh, the orthogonality should be close to 1. Hence the medium mesh grid was used as the main mesh for all future angle of attack investigations.

5.2 Inviscid Flow Study

The BWB aircraft is investigated with ANSYS Fluent utilizing an inviscid flow initially. This investigation is appropriate considering the goals of this study. A preliminary investigation of the overall aircraft aerodynamic shape is desired. The complexity of adding the engines, control surfaces, landing gear, etc. will happen as part of a different project. This thesis is to provide preliminary results detailing the overall aircraft design and to see if it provides the required aerodynamic performance to justify going to the next level in complexity (i.e., adding the engines, etc.). Therefore, an inviscid analysis followed up with some spot checks of the viscous aerodynamic performance is appropriate. All the simulation were run until the solution converged. It took a few hundred iterations for the solutions to converged. The solution for inviscid flow converged until about 11° angle of attack, after which there were some oscillations in the residuals, but the solution was accepted as converged since the lift force and drag force showed small change from the previous iteration. For inviscid flow, simulation was carried out till 15° angle of attack for lift and drag coefficients.

Studying the airflow around the aircraft with an increasing angle of attack is useful in understanding the aircraft behavior in actual flight conditions. The variation of pressure

and Mach number around the geometry are generated for four 2D cross-sections of the aircraft given in Figure:5.1. The cross-section is located at 0.5 m, 6.418m, 18.92 m and 32 m from the centerline respectively.

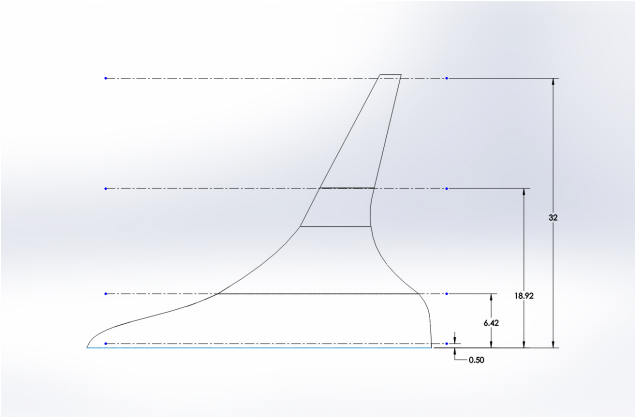

Figure 5.1: 2D Cross-Section Locations on the Aircraft Body

The pressure and Mach number plots for each cross-section are provided for 0, 3, 5, 8, 9, and 10° angle of attack. The Mach number contour plots for each cross-section shows the expected trend, in which the velocity on top of the aircraft is more than at the bottom. This creates a low-pressure zone on top of aircraft and a high-pressure zone on the bottom aircraft. This is expected behavior as the pressure distribution around the aircraft helps in understanding the lift generation.

5.2.1 0° Angle of Attack

The flow properties around the BWB aircraft for 0° angle of attack are given in the following figures. From the pressure field and Mach number contours, we observe that the difference in the velocity profile at the bottom and the top of the aircraft is not very large. This can be observed in the lift force generated in Table: 5.2. It can be observed from Figure: 5.2 that the stagnation point is at the leading edge. The high pressure and the low-pressure region is clearly defined. Accordingly, the low velocity and high-velocity regions

are observed in the velocity plot. The region on the top of aircraft has high velocity as compared to the underside of the aircraft.

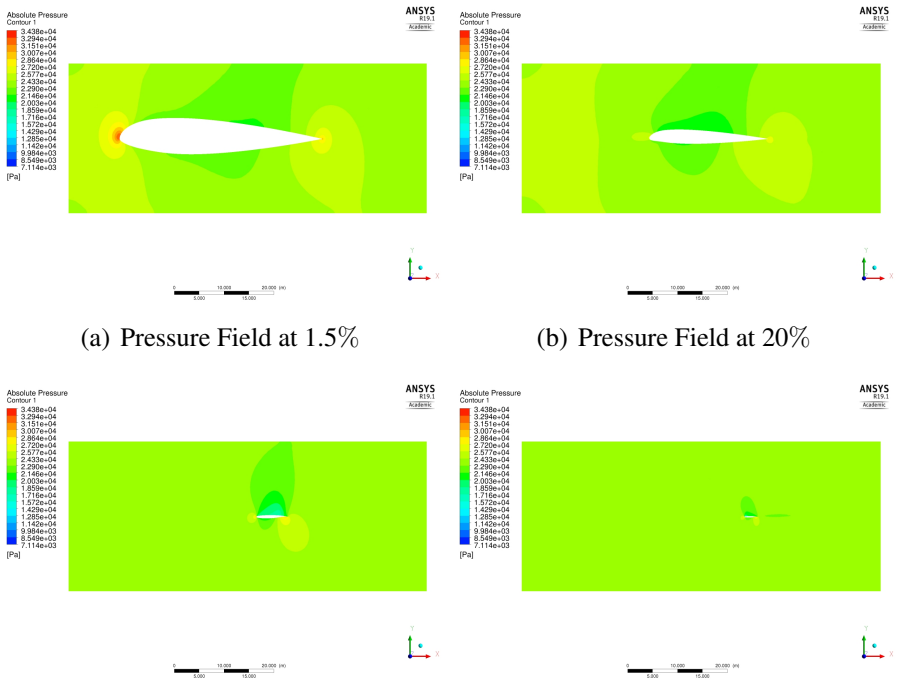

(a) Pressure Field at 1.5%

(b) Pressure Field at 20%

(c) Pressure Field at 58%

(d) Pressure Field at 98%

Figure 5.2: Pressure Field at 0° AoA

5.2.2 3° Angle of Attack

Cruise flight is the longest segment of a commercial flight. Aircraft usually fly at a slight nose up angle of attack during cruise flight. The angle of attack is designed to ensure maximum lift and minimum drag during the cruise. For most aircraft, the cruising angle of attack is small, about 2-4°. Hence a 3° of attack is assumed to be the cruising angle of attack for the BWB aircraft. Increasing the angle of attack results in higher pressure at the bottom surface (Figure: 5.4) compared to 0° angle of attack. The velocity values on the top surface also increase as the angle of attack increases (Figure: 5.5).

Since the pressure difference between the top and the underside of the wing for 3° AoA

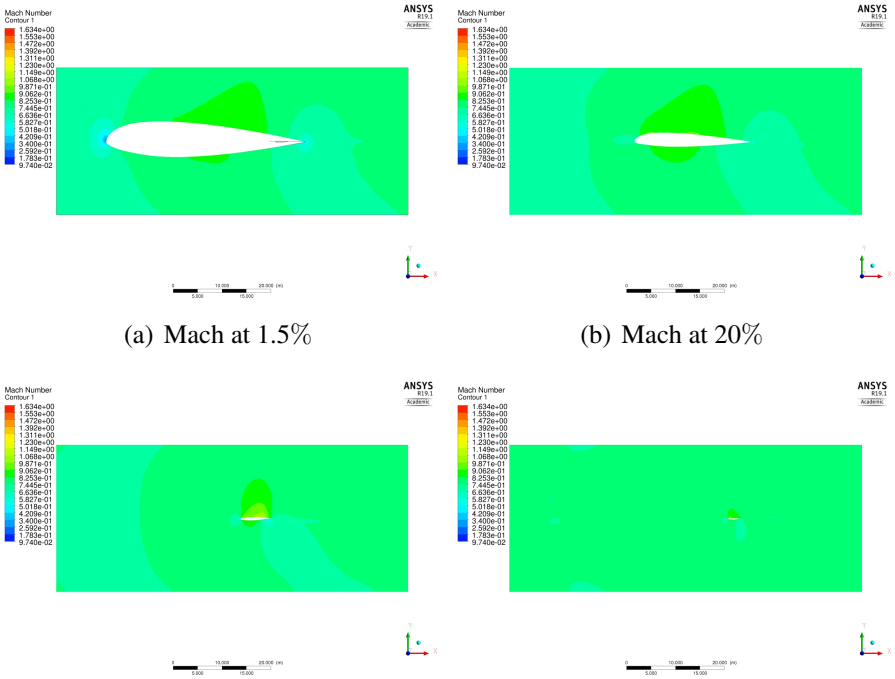

(a) Mach at 1.5%

(b) Mach at 20%

(c) Mach at 58%

(d) Mach at 98%

Figure 5.3: Mach at 0° AoA

is higher as compared to 0° AoA, signaling an increase in lift. It is also worth pointing out that as we move away from the center the velocity and pressure profile change significantly. The change in pressure at the top and bottom surface is more significant as compared to the center fuselage (Figure: 5.4(d) and Figure: 5.4(c)).

The velocity streamlines plot provides a better understanding of the flow around the aircraft. At a low angle of attack, the flow is attached to the airfoil cross-section (Figure:5.6). The velocity streamlines are generated at 2D cross-sections given in Figure: 5.1

Since the geometry was designed without the engines at the wingtip, vortices are generated. The wingtip vortices leads to induced drag generated for the conceptual BWB configuration. Typically this induced drag is removed by the addition of winglets at the wing tips. Winglets will not be used on the BWB TeDP aircraft because the two turbogenerators will be placed at the wing tips. These turbogenerators will act as winglets in

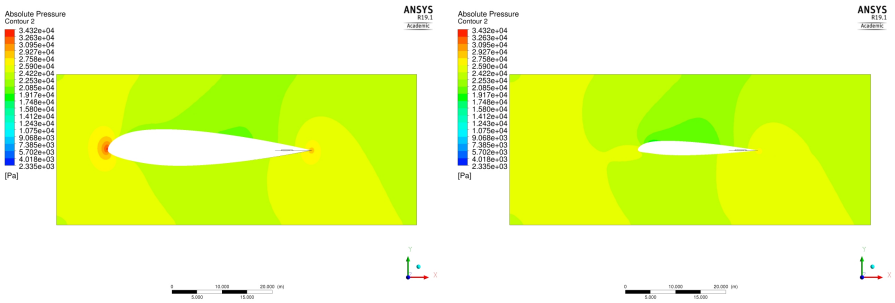

(a) Pressure Field at 1.5%

(b) Pressure Field at 20%

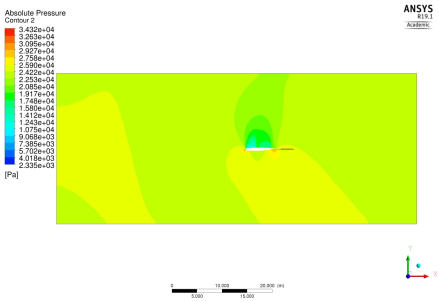

(c) Pressure Field at 58%

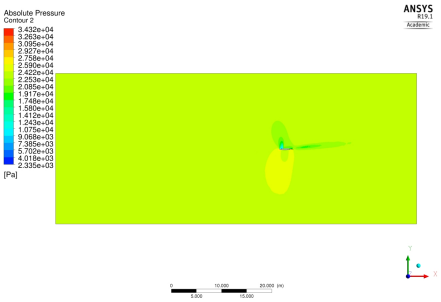

(d) Pressure Field at 98%

Figure 5.4: Pressure Field at 3° AoA

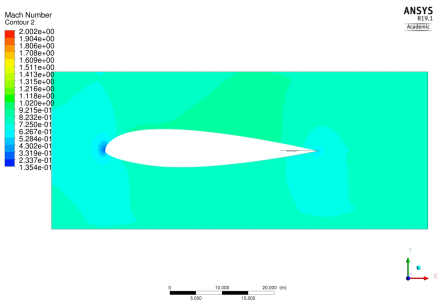

(a) Mach at 1.5%

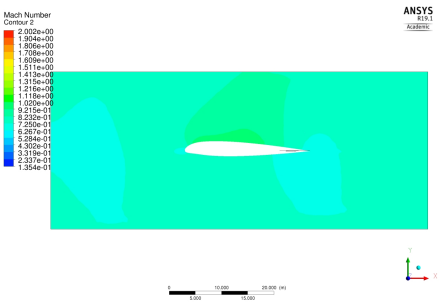

(b) Mach at 20%

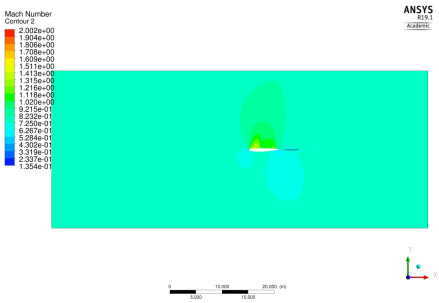

(c) Mach at 58%

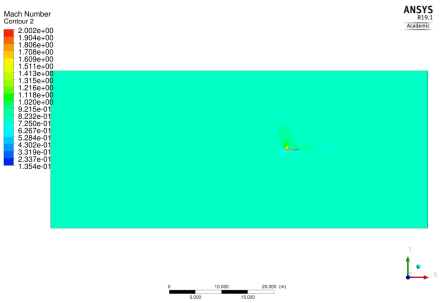

(d) Mach at 98%

Figure 5.5: Mach at 3° AoA

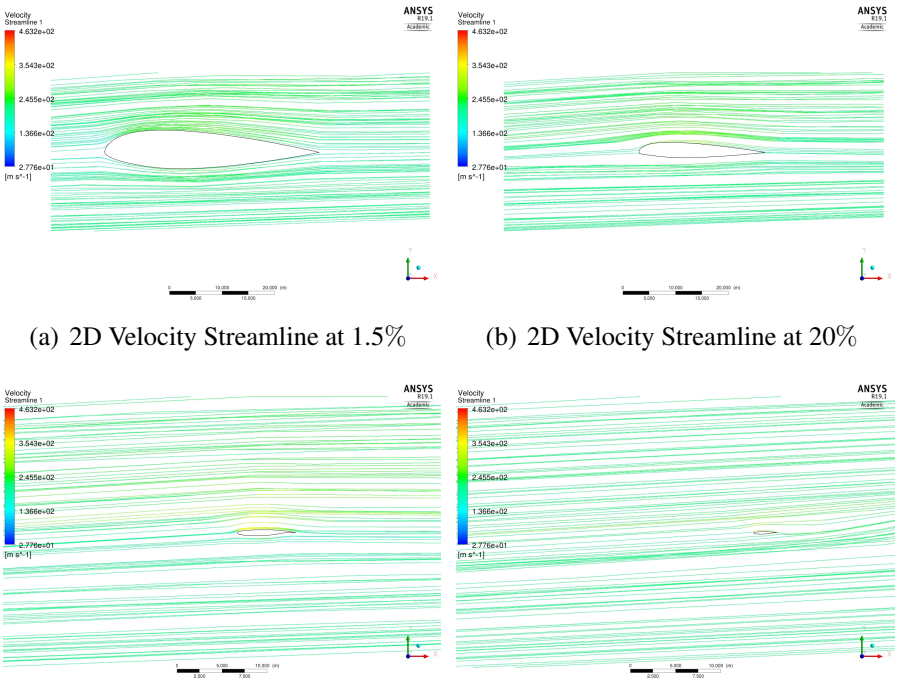

(a) 2D Velocity Streamline at 1.5%

(b) 2D Velocity Streamline at 20%

(c) 2D Velocity Streamline at 58%

(d) 2D Velocity Streamline at 98%

Figure 5.6: 2D Velocity Streamlines at 3° AoA

addition to generating the electrical power required to power the turbofans.

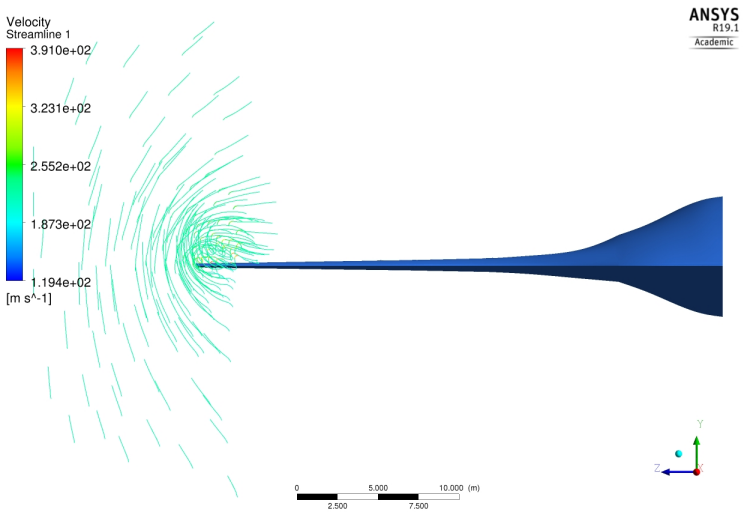

Figure 5.7: Wing Tip Vortices at 3° AoA

5.2.3 5° Angle of Attack

The results for 5° angle of attack are presented next. The pressure profiles of the aircraft show an increase in the pressure difference between the top and the bottom surfaces of the aircraft. The Mach number also increases for the top surface of the aircraft. It is shown that the Mach number reaches the speed of sound for certain regions on the top surface (Figure: 5.9). The continued increase of the vehicle angle of attack results in an increase in the region of supersonic flow on the upper surface on the wings.

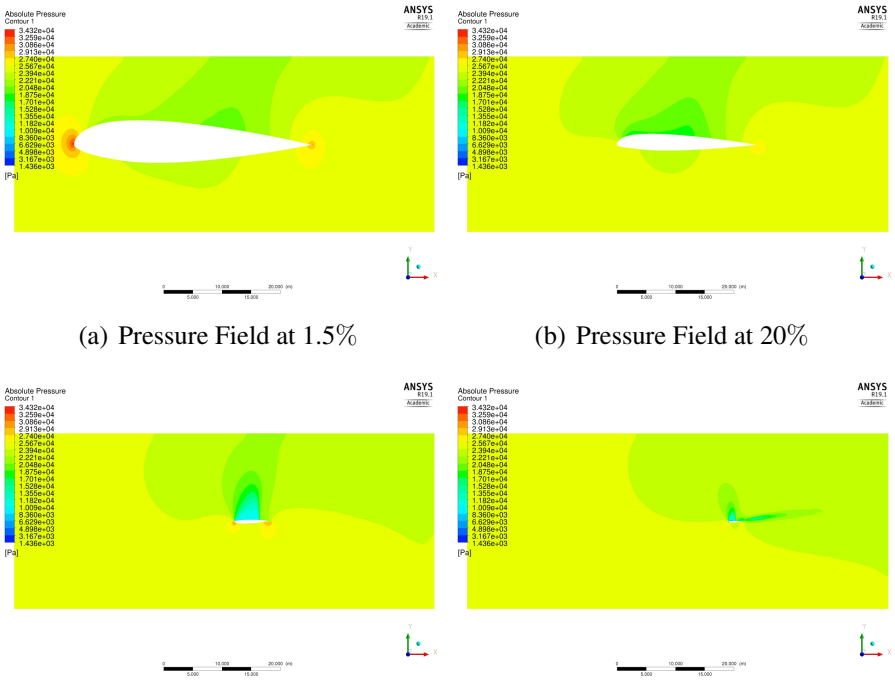

(a) Pressure Field at 1.5%

(b) Pressure Field at 20%

(c) Pressure Field at 58%

(d) Pressure Field at 98%

Figure 5.8: Pressure Field at 5° AoA

It is observed that the pressure contours and Mach number contours change significantly with increasing angle of attack. The pressure region on the bottom surface increases with the increasing angle of attack indicating an increase in lift. In regards to the Mach number, the velocity at the top surface reaches the speed of sound at certain regions with an increase in the angle of attack. The high-velocity region has a significant increase in

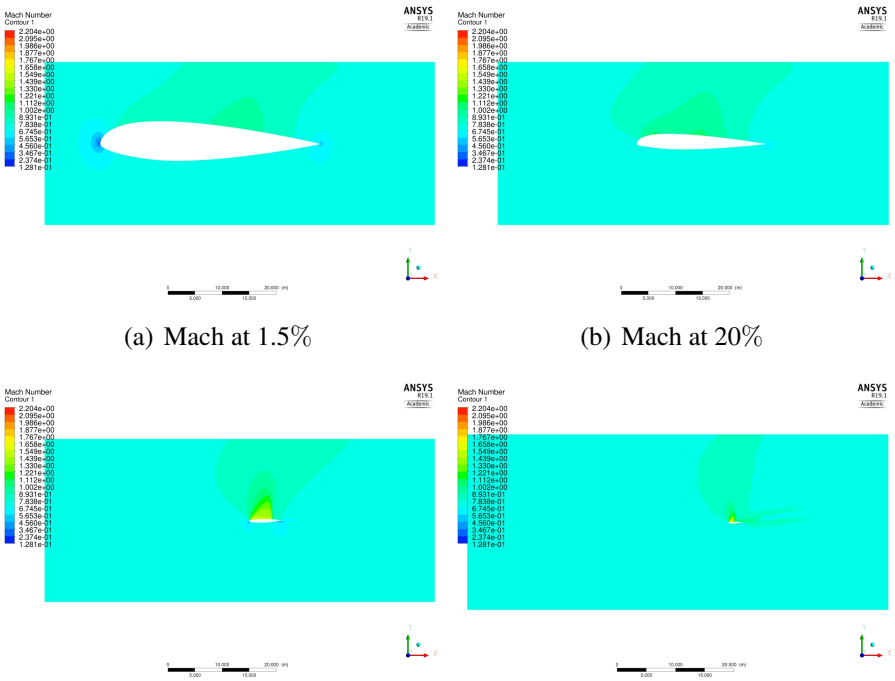

(a) Mach at 1.5%

(b) Mach at 20%

(c) Mach at 58%

(d) Mach at 98%

Figure 5.9: Mach at 5° AoA

velocity compared to the actual velocity. Also, the area for high-velocity region increases with angle of attack. This leads to an increase in drag at higher Mach number. The velocity or Mach number plot for 8°, 9°, and 10° angle of attack are presented in Figure 5.10 thru Figure 5.12 respectively.

It is observed that there is a small normal shock generated on the outer wing at 8°. The normal shock increases the aerodynamic losses generated by an increase in the angle of attack. The shock region increases and grows stronger as the angle of attack increases. This leads to flow separation eventually stalling the aircraft. The low or reversed velocity region characterizes the flow separation region. The low-velocity region increases with the angle of attack. These characteristics are observed in Figure: 5.11(c), and Figure: 5.11(d) for 9° and Figure: 5.12(c), and Figure: 5.12(d) for 10°.

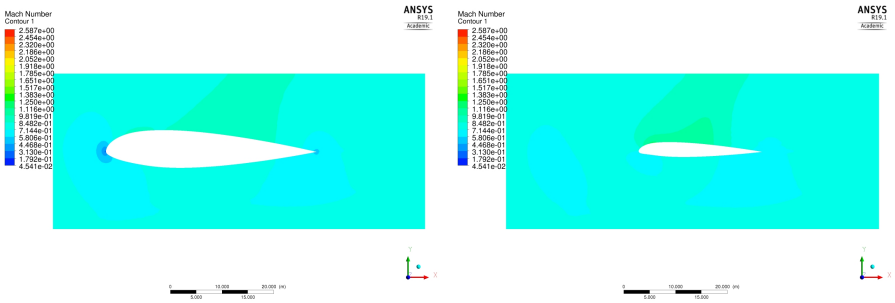

(a) Mach at 1.5%

(b) Mach at 20%

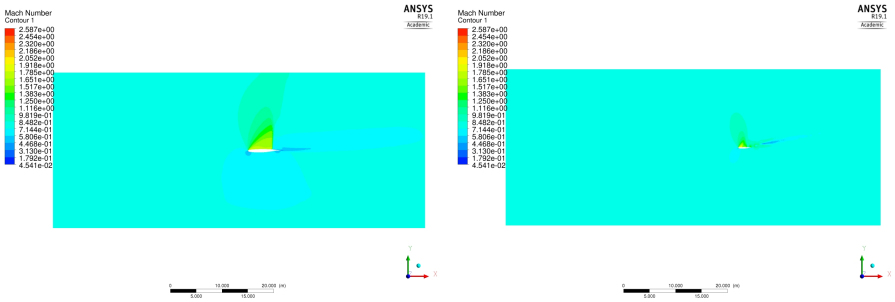

(c) Mach at 58%

(d) Mach at 98%

Figure 5.10: Mach at 8° AoA

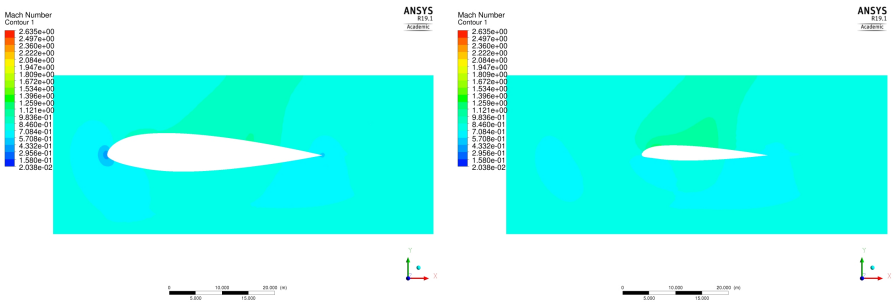

(a) Mach at 1.5%

(b) Mach at 20%

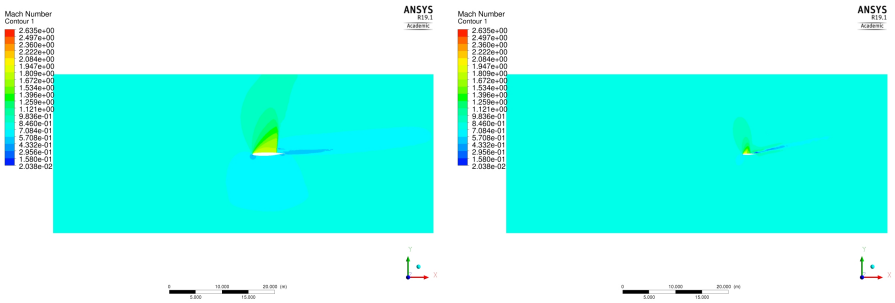

(c) Machat 58%

(d) Mach 98%

Figure 5.11: Mach at 9° AoA

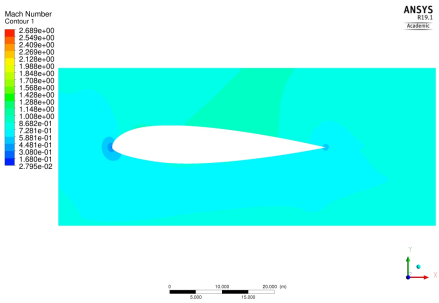

(a) Mach at 1.5%

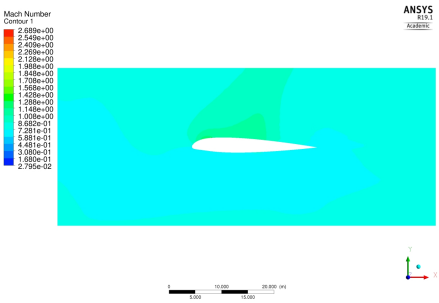

(b) Mach at 20%

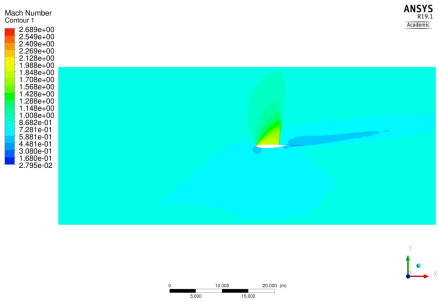

(c) Mach at 58%

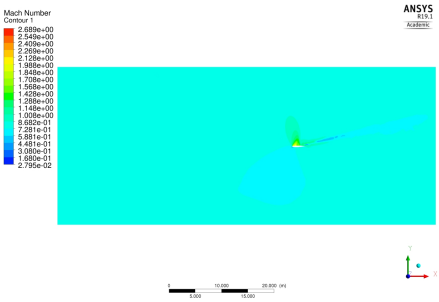

(d) Mach at 98%

Figure 5.12: Mach at 10° AoA

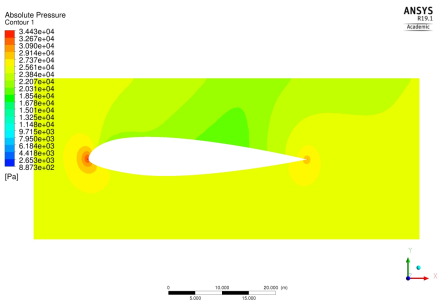

(a) Pressure Field at 1.5%

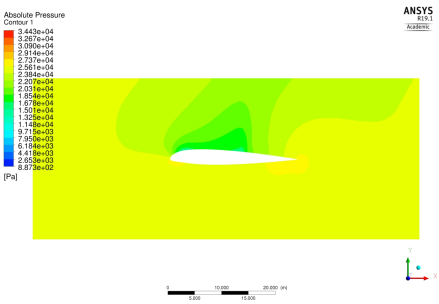

(b) Pressure Field at 20%

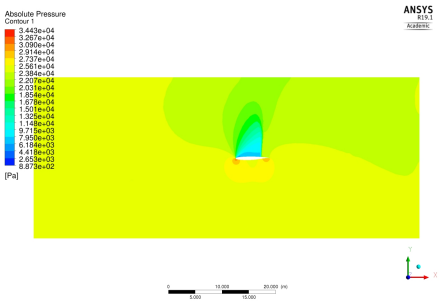

(c) Pressure Field at 58%

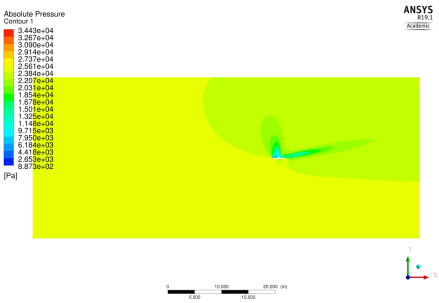

(d) Pressure Field at 98%

Figure 5.13: Pressure Field at 8° AoA

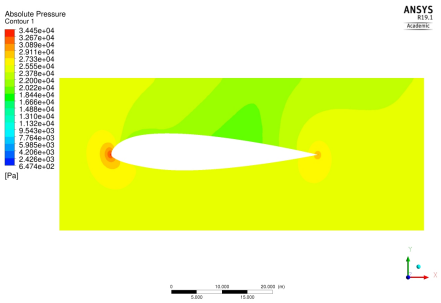

(a) Pressure Field at 1.5%

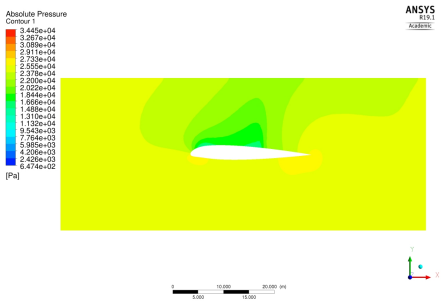

(b) Pressure Field at 20%

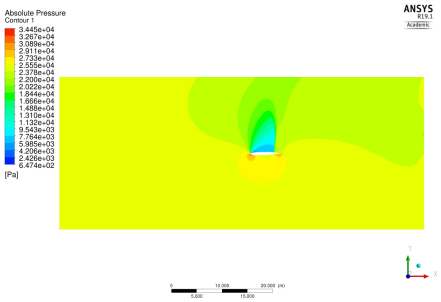

(c) Pressure Field at 58%

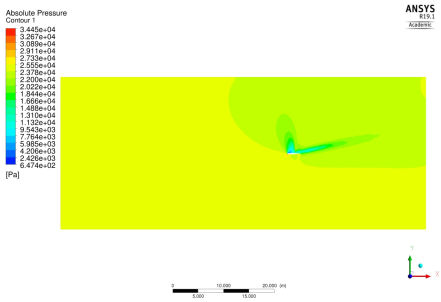

(d) Pressure Field at 98%

Figure 5.14: Pressure Field at 9° AoA

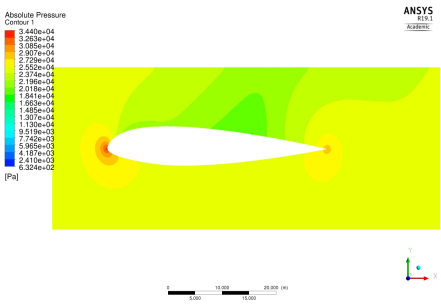

(a) Pressure Field at 1.5%

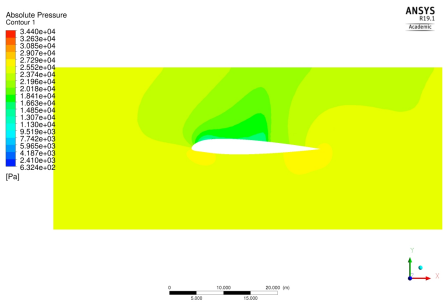

(b) Pressure Field at 20%

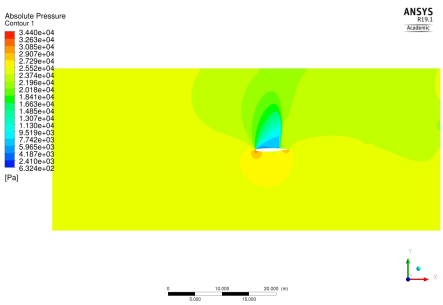

(c) Pressure Field at 58%

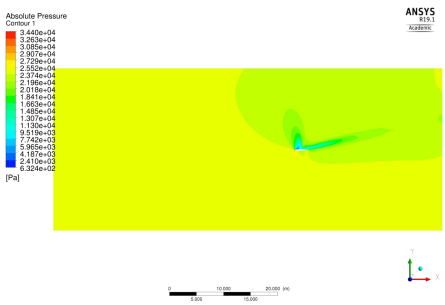

(d) Pressure Field at 98%

Figure 5.15: Pressure Field at 10° AoA

The pressure contours for 8°, 9°, and 10° angle of attack are presented in Figure 5.13 - Figure 5.15 respectively.

The pressure coefficient for each 2D sections given in Figure: 5.1 are plotted for 0, 3, 5 and 8° angle of attack. The increase in lift is evident as the area between the curves increases. The coefficient of pressure plots are given in Figure 5.16 - Figure 5.19. For the four different spanwise locations across the BWB aircraft. It is evident that at 1.5% span (i.e., near the aircraft centerline) that there are no shocks present in the flow for all the angles of attack. At 20% Figure 5.17, a normal shock first occurs at an angle of attack of 8, but it is not present at any of the lower angle of attacks. Next at 58% Figure 5.18, the normal shock is present for all angles but 0. Finally, Figure 5.19 shows a normal shock for all angles of attack at 98% span. Also at 98% span, the effect of the tip vortex is evident in the distorted pressure distributions.

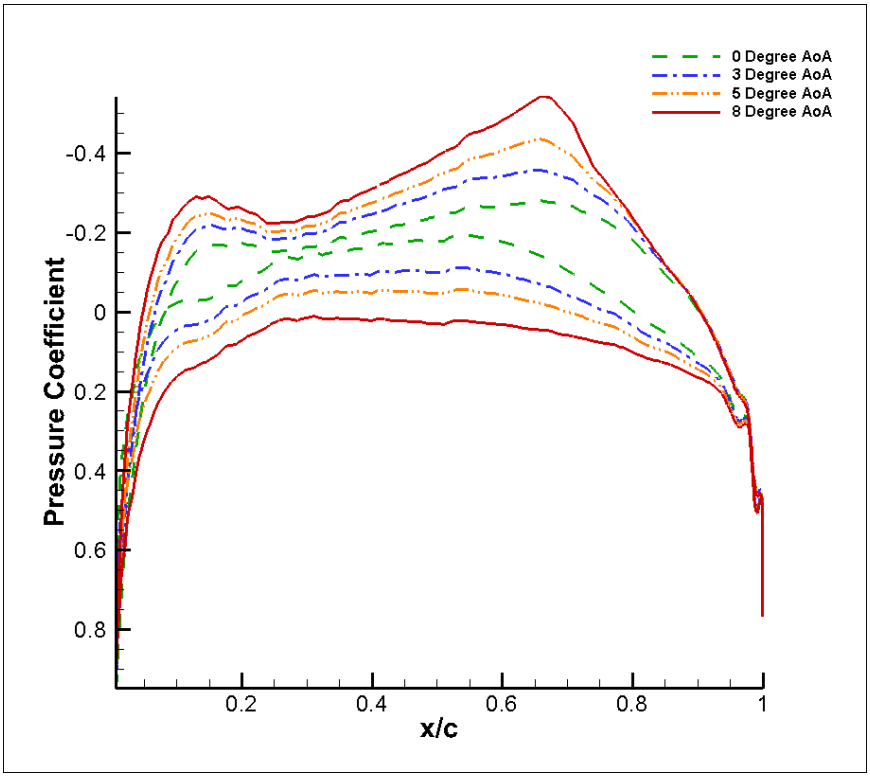

Figure 5.16: Pressure Coefficient Distribution on Top and Bottom of the Aircraft at 1.5%

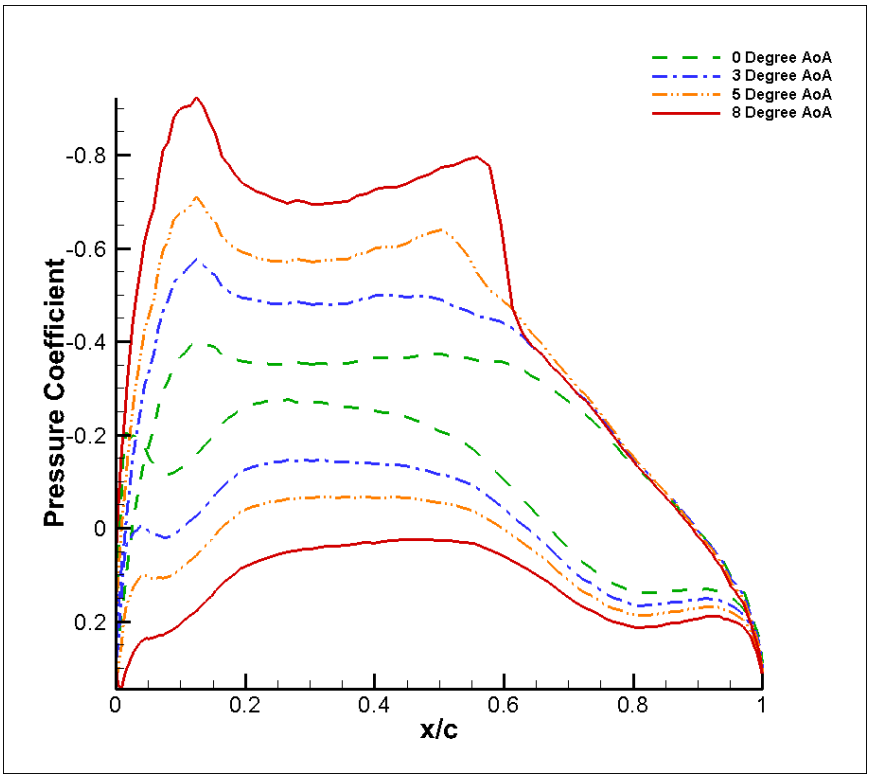

Figure 5.17: Pressure Coefficient Distribution on Top and Bottom of the Aircraft at 20%

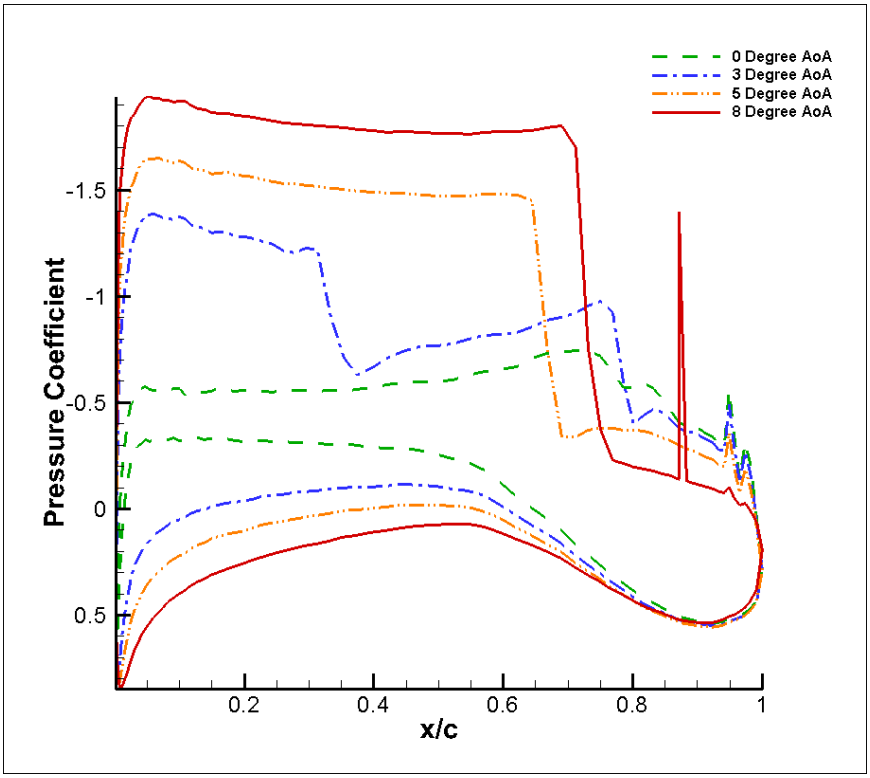

Figure 5.18: Pressure Coefficient Distribution on Top and Bottom of the Aircraft at 58%

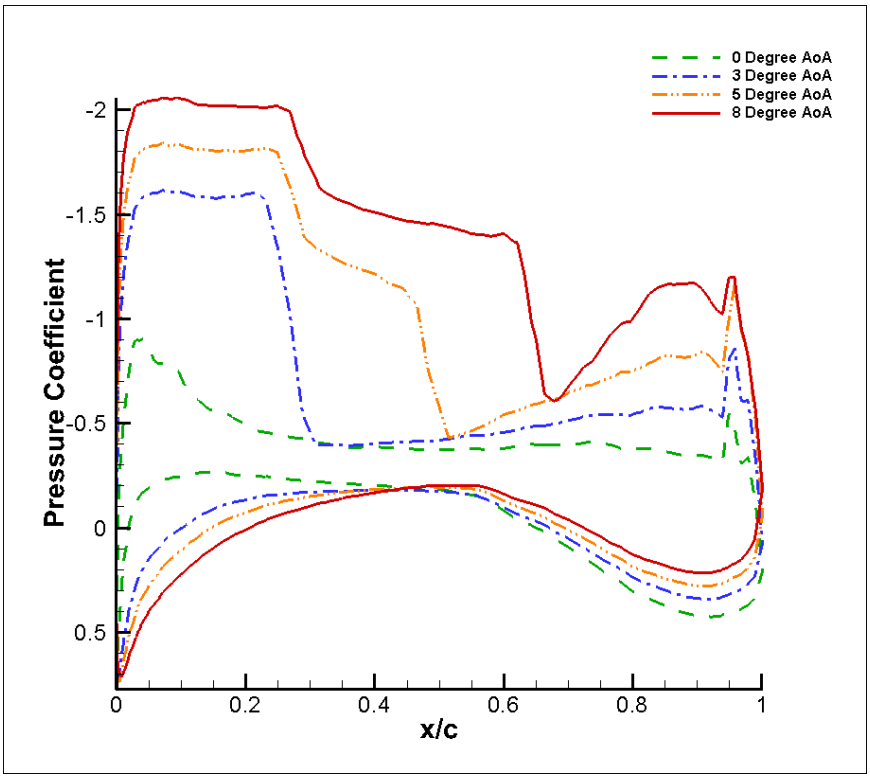

Figure 5.19: Pressure Coefficient Distribution on Top and Bottom of the Aircraft at 98%

5.3 Viscous Flow Study

A viscous analysis of the BWB aircraft was obtained for a few angles of attack. It is more expensive to do a viscous analysis both in terms of the time taken to generate a viscous model and the computational resources required to perform the analysis. At this stage in aircraft design, it is appropriate to do a few viscous studies to ensure no significant flow physics is being missed. For the viscous flow analysis, the $k - \omega$ SST turbulence model was used. The residuals took longer to converge compared to inviscid flow. It took some 800 - 2500 iterations for all the residuals to converged. The viscous flow analysis accounts for flow very close to the aircraft surface since it is considering the boundary layer effects. The y-plus value plot shows that the value is in the specified region of $y^+ < 300$. The y^+ contour plot can be found in Figure: 5.20 and Figure:5.21). This means the turbulence model is being implemented properly. The analysis was performed for 0°, 3°, and 5° angle of attack.

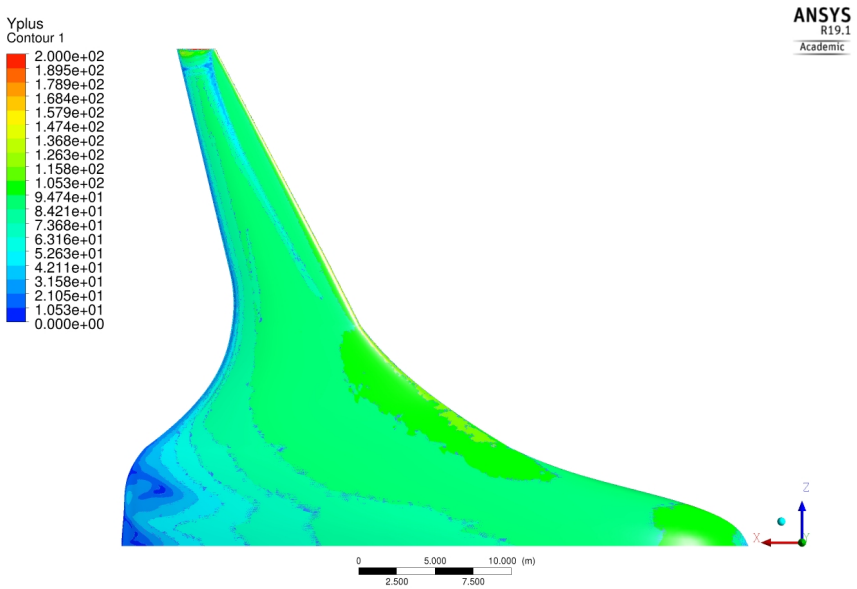

Figure 5.20: y-plus Contour Plot for 3° AoA

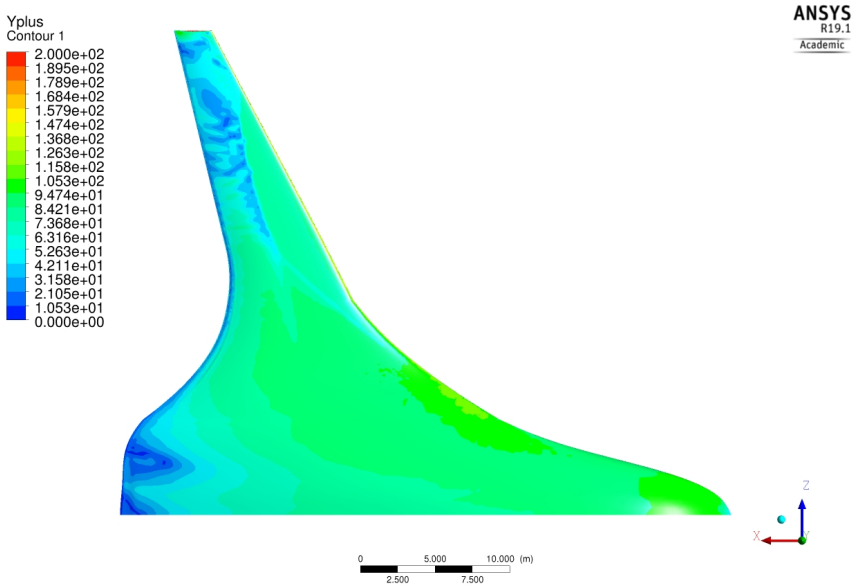

Figure 5.21: y-plus Contour Plot for 5° AoA

5.3.1 Pressure Distribution

The pressure distribution is represented at the four 2D cross-sections represented in Figure. 5.1. The pressure contours show three major areas: the stagnation area, the low-pressure region, and the high-pressure region as observed in the inviscid analysis. The low-pressure region is at the top of the aircraft surface and the high-pressure region at the lower surface. As the angle of attack is increased the pressure difference between the two regions increases to a certain point. The difference observed in the viscous plots when compared to the inviscid analysis is that the flow near the aircraft wall is more defined to understand the aerodynamic effects better. The pressure distribution for 0°, 3°, and 5° angle of attack is given in Figure:5.22 thru Figure:5.24.

It is observed that the low-pressure region on the top surface increases in extent and intensity as the angle of attack is increased. The high-pressure region also increases with the angle of attack. This leads to an increase in pressure difference thus increasing the lift. This phenomenon is better understood in the pressure coefficient graphs. In Figure. 5.25 -

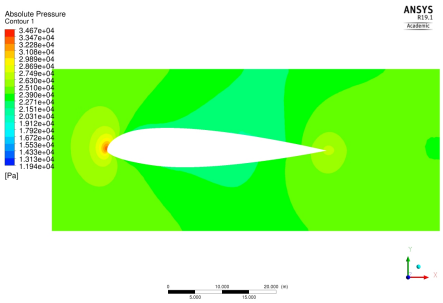

(a) Pressure Field at 1.5%

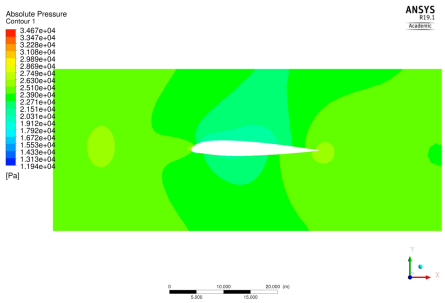

(b) Pressure Field at 20%

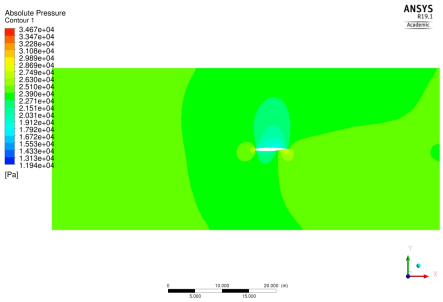

(c) Pressure Field at 58%

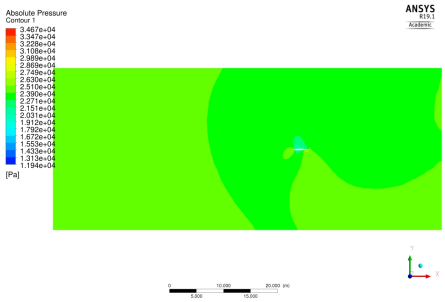

(d) Pressure Field at 98%

Figure 5.22: Pressure Field at 0° AoA

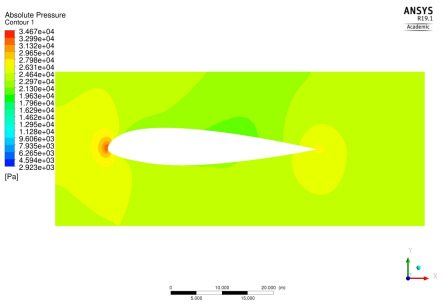

(a) Pressure Field at 1.5%

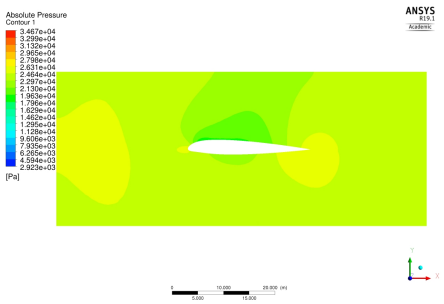

(b) Pressure Field at 20%

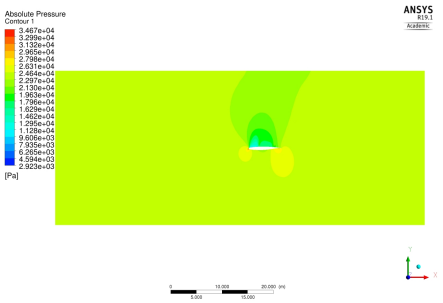

(c) Pressure Field at 58%

(d) Pressure Field at 98%

Figure 5.23: Pressure Field at 3° AoA

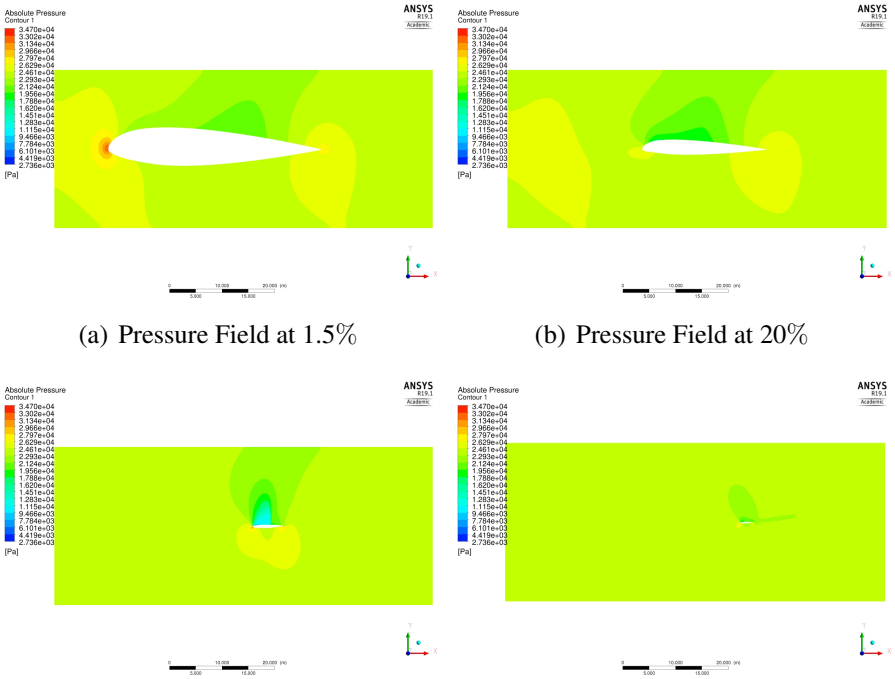

(a) Pressure Field at 1.5%

(b) Pressure Field at 20%

(c) Pressure Field at 58%

(d) Pressure Field at 98%

Figure 5.24: Pressure Field at 5° AoA

Figure. 5.28, the region below the x-axis increases with the angle of attack thus pushing the wing upwards. This is expected and was already observed in the inviscid flow analysis. The difference here is that area between the curve for an angle of attack is less when compared to inviscid flow. Hence there is a decrease in lift force generated for the viscous flow. Also, the normal shock is observed on the outer wing at 3° and 5° angle of attack.

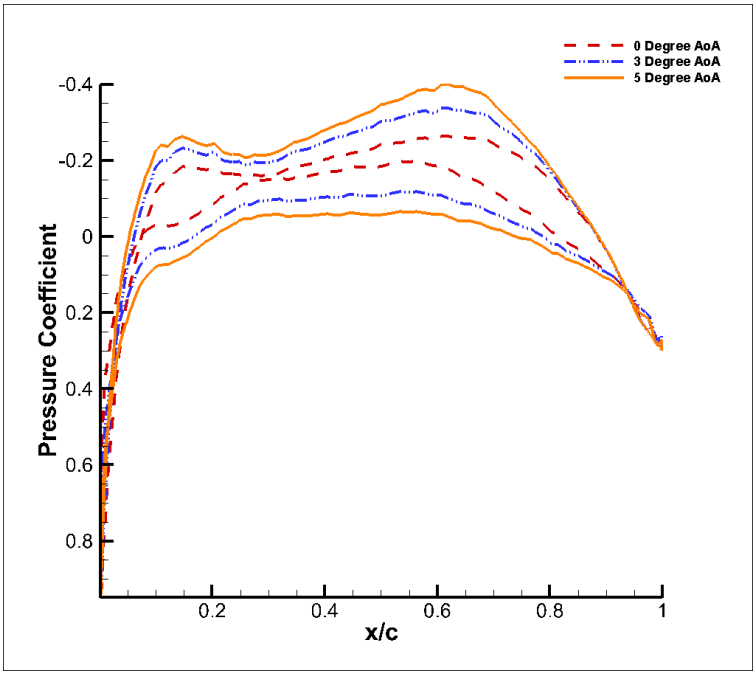

Figure 5.25: Pressure Coefficient Distribution on Top and Bottom of the Aircraft at 1.5% for Viscous Flow

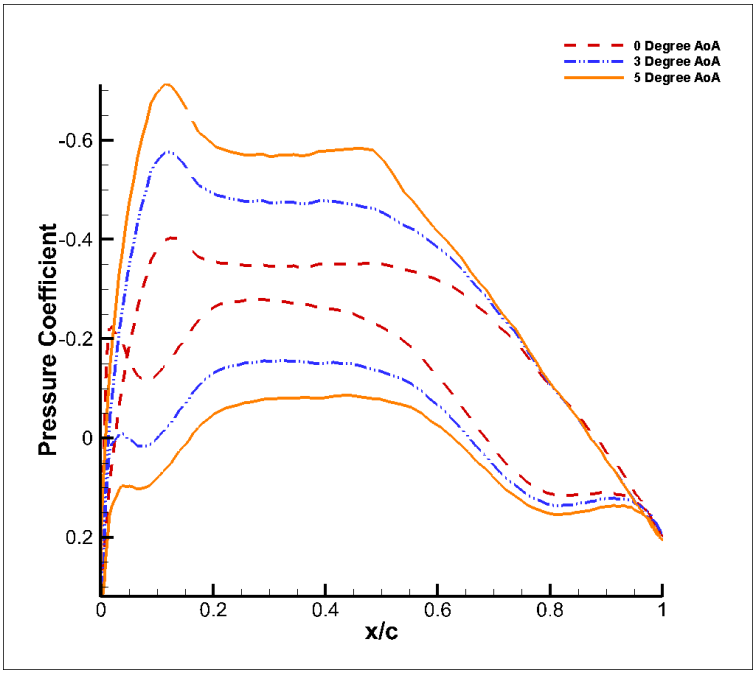

Figure 5.26: Pressure Coefficient Distribution on Top and Bottom of the Aircraft at 20% for Viscous Flow

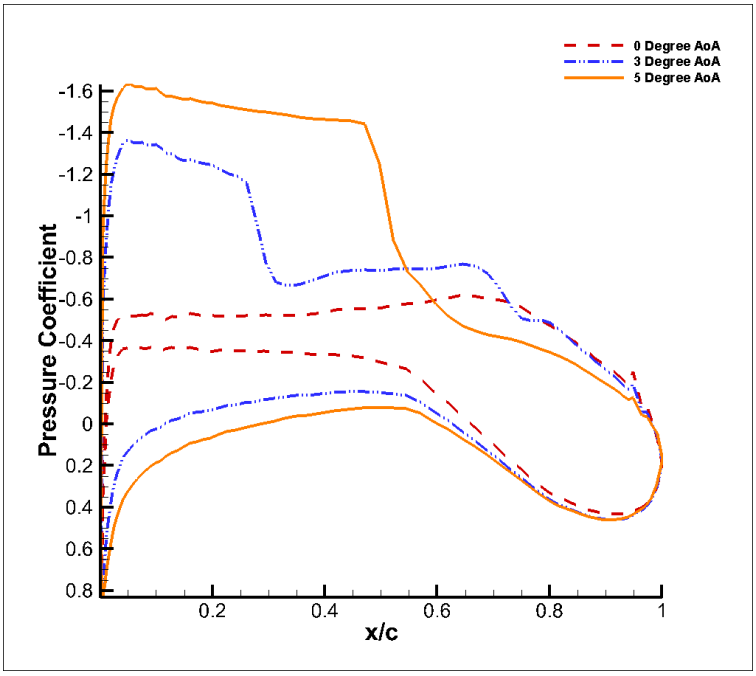

Figure 5.27: Pressure Coefficient Distribution on Top and Bottom of the Aircraft at 58% for Viscous Flow

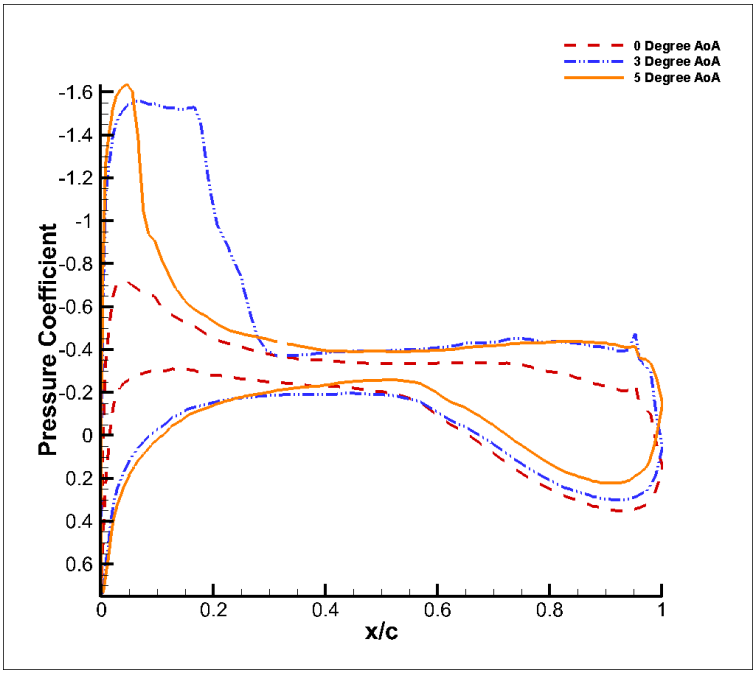

Figure 5.28: Pressure Coefficient Distribution on Top and Bottom of the Aircraft at 98% for Viscous Flow

5.3.2 Velocity Distribution

The velocity distribution shows the flow around the wings. Zero velocity point is observed at the leading edge and the high-velocity region on the top aircraft surface. This compliments the low-pressure region observed on the top surface. As observed in the inviscid flow the magnitude of velocity increases over the top surface as the angle of attack is increased. A normal shock wave is also created on the top surface of the outer wing at 5° AoA.

The shock is prominently visible on the top surface moving towards the wingtip. The velocity distribution is presented in Figure: 5.29 thru Figure: 5.31. To study the boundary layer flow, we use the velocity streamline. For the viscous flows, 2D streamlines were plotted and presented in Figure: 5.32 thru Figure: 5.34. We observe that the velocity streamlines move smoothly over the aircraft surface. However reverse flow and flow separation are observed near the trailing edge. At 0° AoA a reverse flow is visible with a small vortex region at the trailing edge in Figure: 5.35. The flow separation region at the trailing edge increases with angle of attack. Some sections of the aircraft with the boundary layer are presented in the Figure: 5.37 - Figure: 5.40 . We can observe that at the wall, the flow velocity is low and increases in magnitude as we move further away from the aircraft surface. The velocity eventually reaches the local free stream velocity in that region. These effects are observed for viscous flow analysis.

In Figure: 5.40, we observe near the aircraft wall, just after the normal shock wave there is some reverse flow with flow separation at the aircraft surface. The flow reattaches itself as we move further downstream. In transonic flow analysis, this flow physics is complicated to predict. The ANSYS Fluent CFD model does a good job of predicting this flow feature with the turbulence model.

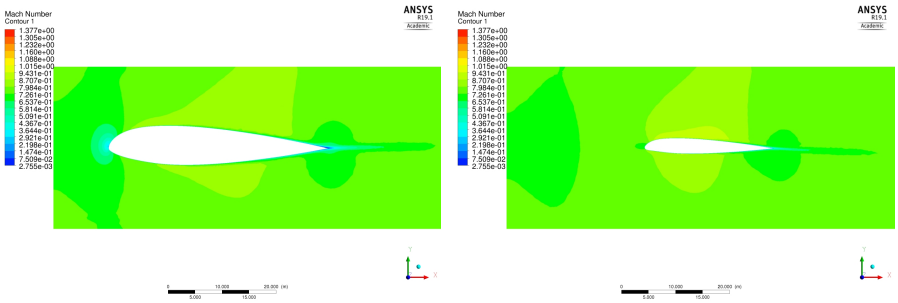

(a) Mach at 1.5%

(b) Mach at 20%

(c) Mach at 58%

(d) Mach at 98%

Figure 5.29: Mach at 0° AoA

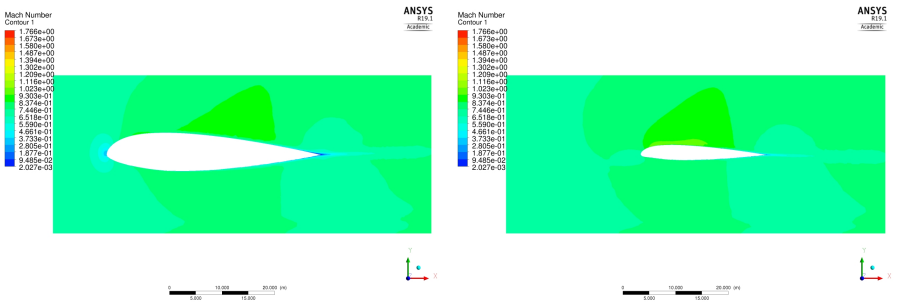

(a) Mach at 1.5%

(b) Mach at 20%

(c) Mach at 58%

(d) Mach at 98%

Figure 5.30: Mach at 3° AoA

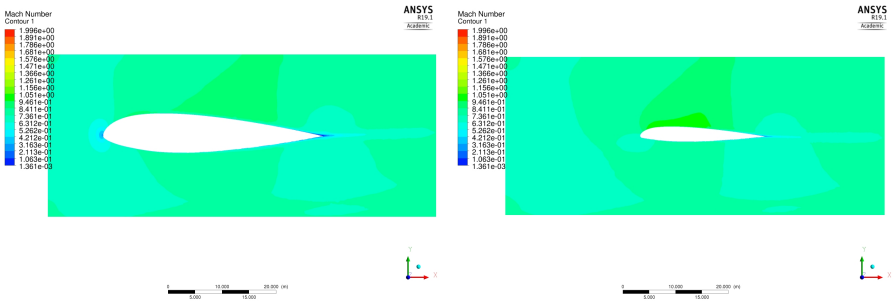

(a) Mach at 1.5%

(b) Mach at 20%

(c) Mach at 58%

(d) Mach at 98%

Figure 5.31: Mach at 5° AoA

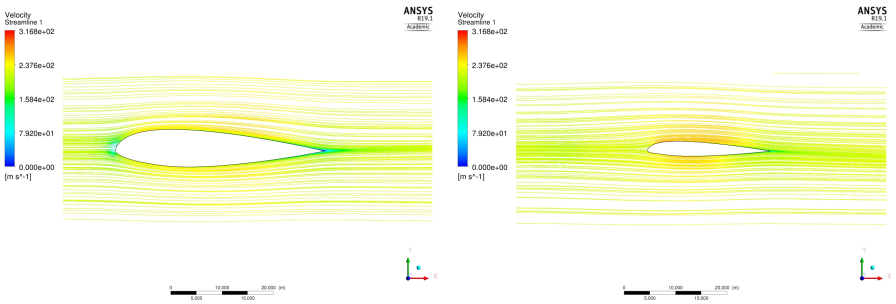

(a) 2D Velocity Streamline at 1.5%

(b) 2D Velocity Streamline at 20%

(c) 2D Velocity Streamline at 58%

(d) 2D Velocity Streamline at 98%

Figure 5.32: 2D Velocity Streamlines at 0° AoA

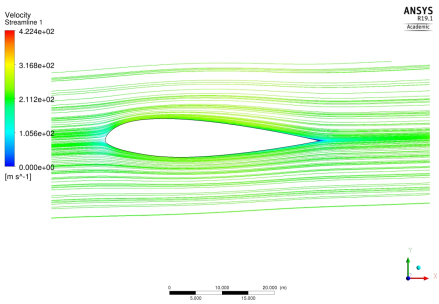

(a) 2D Velocity Streamline at 1.5%

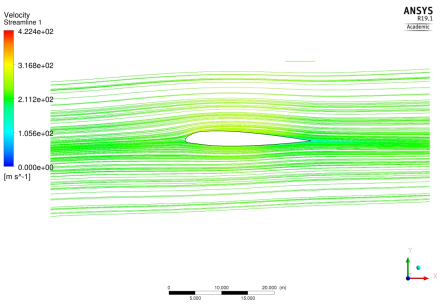

(b) 2D Velocity Streamline at 20%

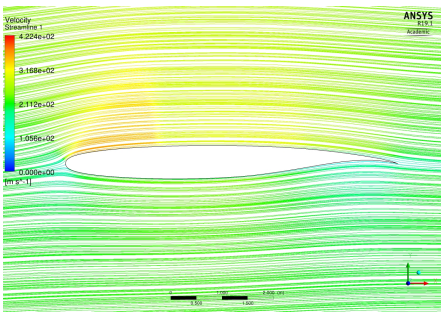

(c) 2D Velocity Streamline at 58%

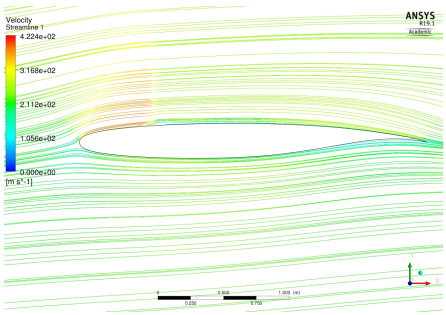

(d) 2D Velocity Streamline at 98%

Figure 5.33: 2D Velocity Streamlines at 3° AoA

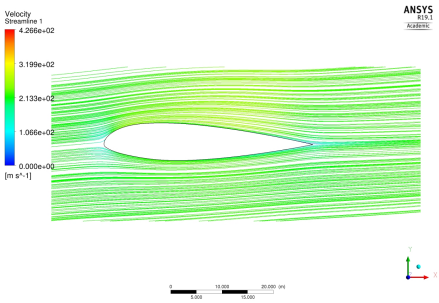

(a) 2D Velocity Streamline at 1.5%

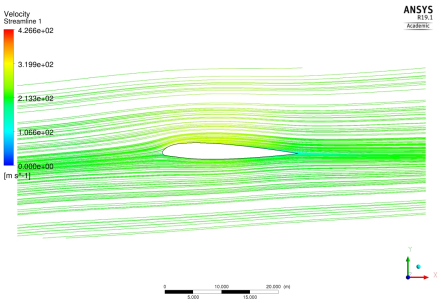

(b) 2D Velocity Streamline at 20%

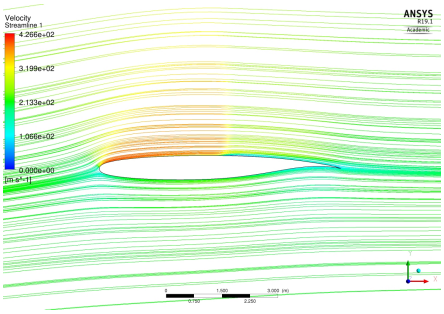

(c) 2D Velocity Streamline at 58%

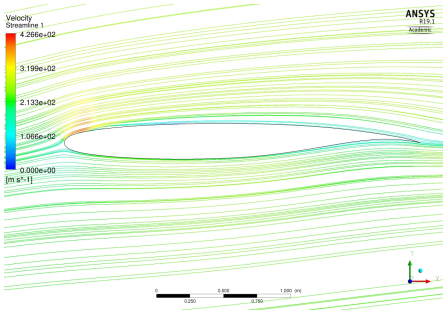

(d) 2D Velocity Streamline at 98%

Figure 5.34: 2D Velocity Streamlines at 5° AoA

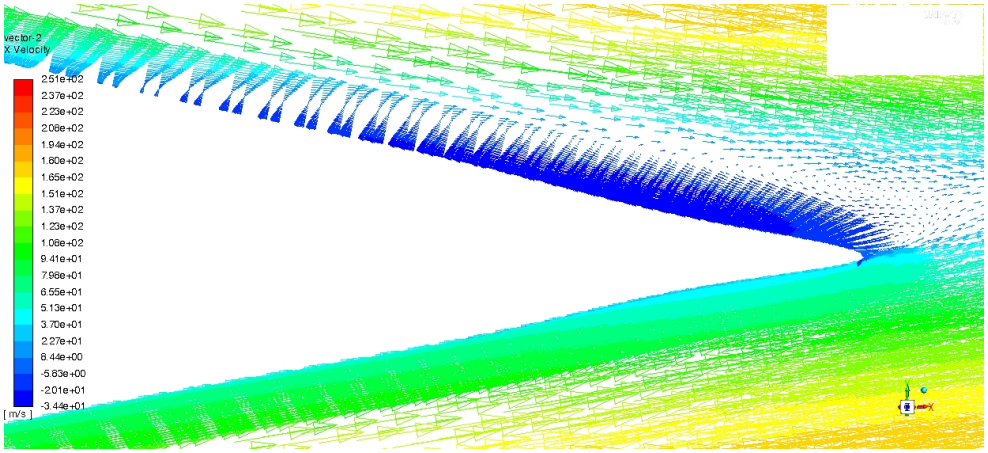

Figure 5.35: Velocity Vector at 1.5% from Centerline at the trailing edge for 0° AoA

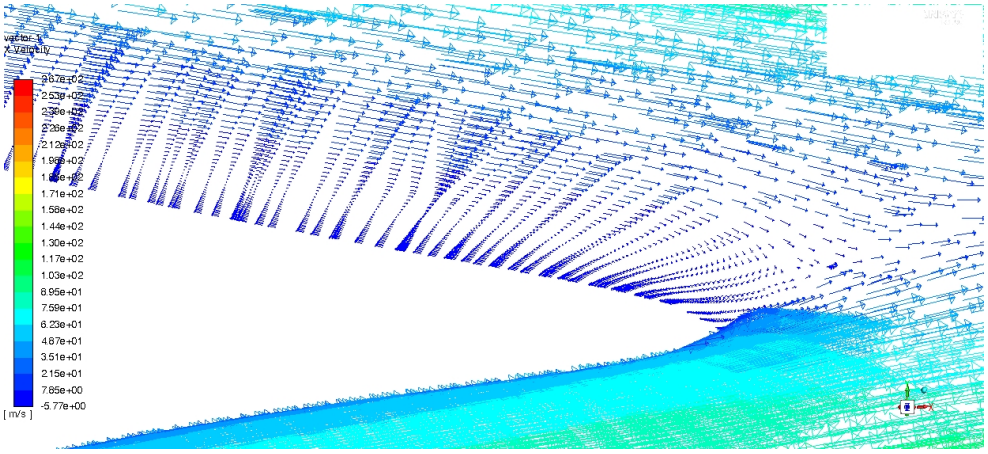

Figure 5.36: Velocity Vector at 1.5% from Centerline at the trailing edge for 5° AoA

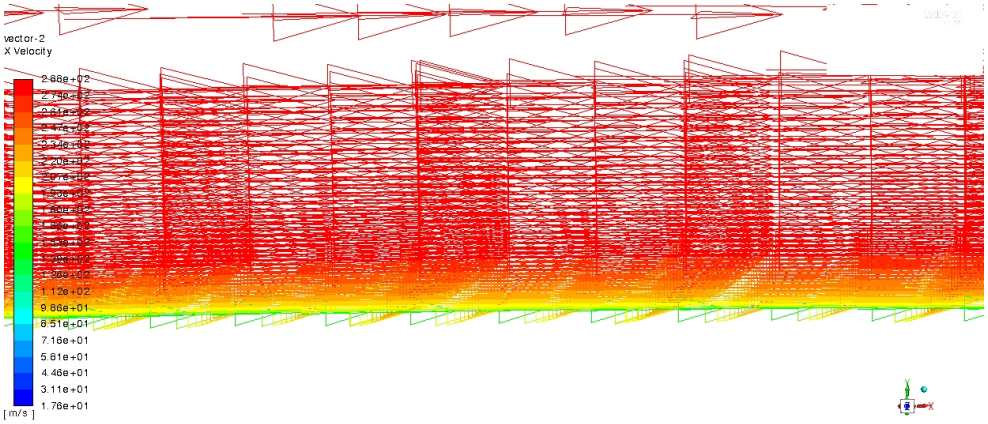

Figure 5.37: Velocity Vector at 58% from Centerline for 0° AoA

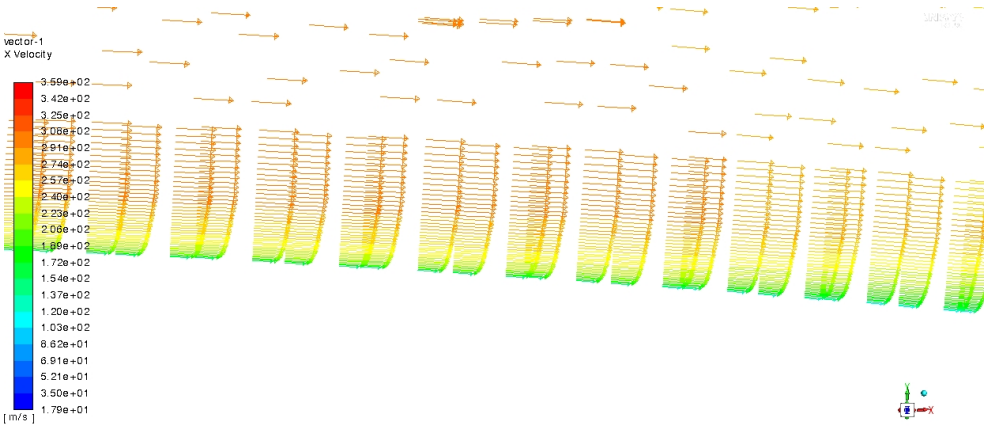

Figure 5.38: Velocity Vector at 1.5% from Centerline for 3° AoA

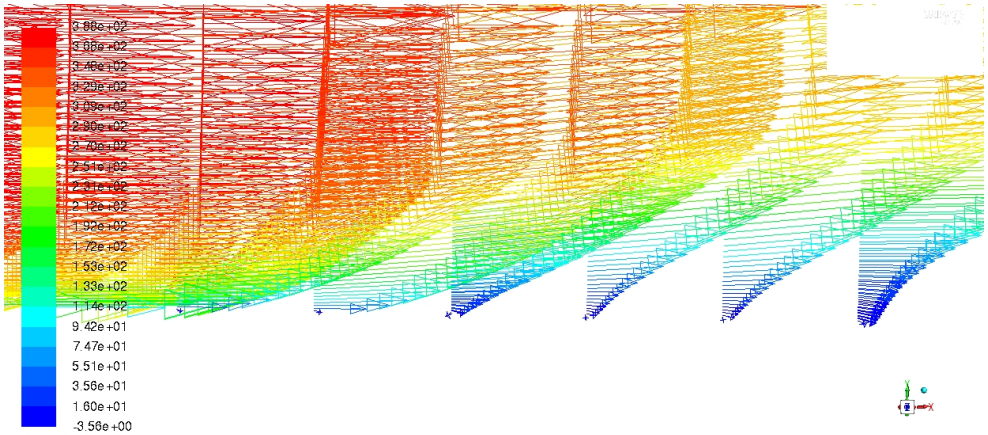

Figure 5.39: Velocity Vector at 58% from Centerline for 5° AoA

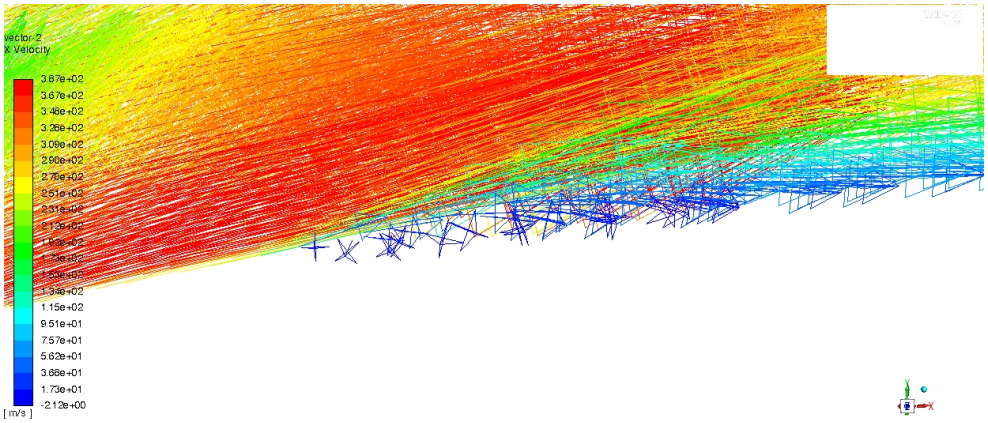

Figure 5.40: Velocity Vector at 98% from Centerline for 5° AoA

5.4 Aerodynamic Force Coefficients

The lift and drag force were obtained from the ANSYS Fluent CFD model are for the half aircraft model. The lift coefficient (C_L) and drag coefficient (C_D) were calculated using Equations 4.2 and 4.3. We use only half of the aircraft's total area since the lift force, and the drag force is also half. For calculating the coefficients, we need the density and velocity values at 35000 ft altitude. The density varies as we go higher in altitude thus changing the speed of sound. Since we are using the pressure far-field boundary conditions, we input the flow velocity in terms of Mach number. Hence the Mach number needs to be converted to free stream velocity using density obtained from ANSYS Fluent for an ideal gas. The density for Ideal gas at 35000 ft is ρ = 0.3795 $kg.m^{-3}$. This gives the velocity for 0.75 M as V = 223.656 m^2. The values for C_L and C_D for inviscid flow are provided in Table: 5.2 and for the viscous flow in Table: 5.3.

Table 5.2: Aerodynamic Coefficients for Inviscid Flow

Angle of - Attack $(^\circ)$	**Lift Force** (N)	**Coefficient of Lift**	**Drag Force**(N)	**Coefficient of Drag**
0°	973,292	0.216	49,496	0.011
3°	1,922,849	0.428	119,211	0.026
5°	2,580,782	0.575	217,625	0.048
8°	3,335,057	0.743	422,483	0.094
9°	3,501,471	0.780	493,477	0.110
10°	3,606,306	0.803	557,840	0.124
11°	3,738,345	0.833	633,633	0.141
12°	2,288,114	0.510	446,913	0.099
15°	2,217,356	0.494	612,532	0.136

The lift coefficient increases gradually with increasing angle of attack until it reaches 11° at which point a drop in lift appears. (Figure:5.41). Thus the maximum lift coefficient for the designed BWB aircraft is $C_{l_{max}}$ = 0.833. Comparing Figure:5.41 against the lift vs. AoA graph from Cranfield University for NASA N3-X, a close resemblance for the $C_{l_{max}}$ and the stall angle is observed. It is important to remember that the conceptual BWB and

the NASA N3-X geometry uses different airfoil sections and hence some differences are expected.

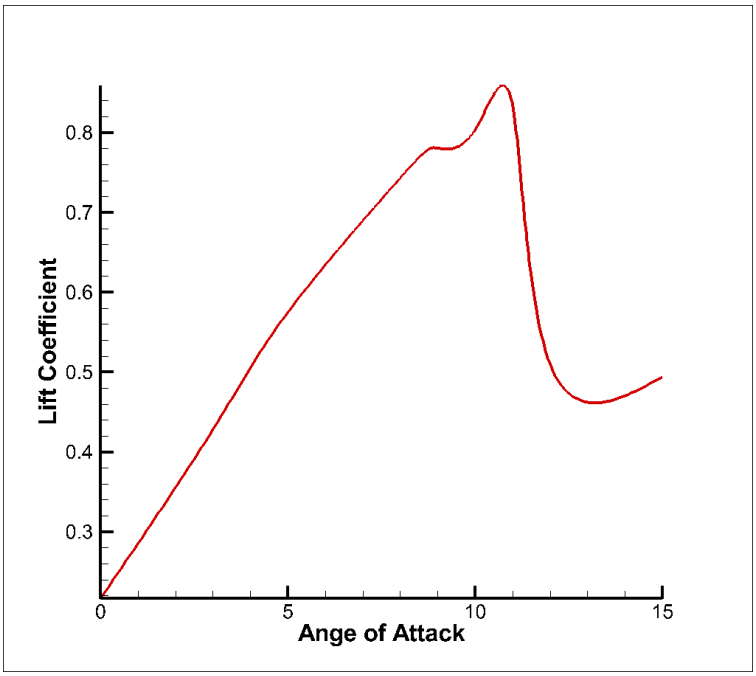

Figure 5.41: Lift Coefficient vs AoA for Inviscid Flow

The drag coefficient increases as the angle of attack is increased. As the flow analysis showed, the separation region grows with the increase in the angle of attack the increase in separation results in an increase in drag. An anomaly in the drag curve is observed after the stall angle.

The L/D ratio is an essential parameter in understanding the aerodynamic performance of an aircraft. For the designed BWB configuration, the L/D for the cruise condition is 16.12. The Airbus 380 has an L/D of 13.74[17]. Hence the L/D ratio is improved by 15%. The L/D ratio can be improved further with boundary layer ingestion and the engines at the wingtips acting as winglets.

It is observed that the lift coefficient decreases for the viscous flow analysis. The decrease is attributed to the effects of the boundary layer and normal shock interaction at the

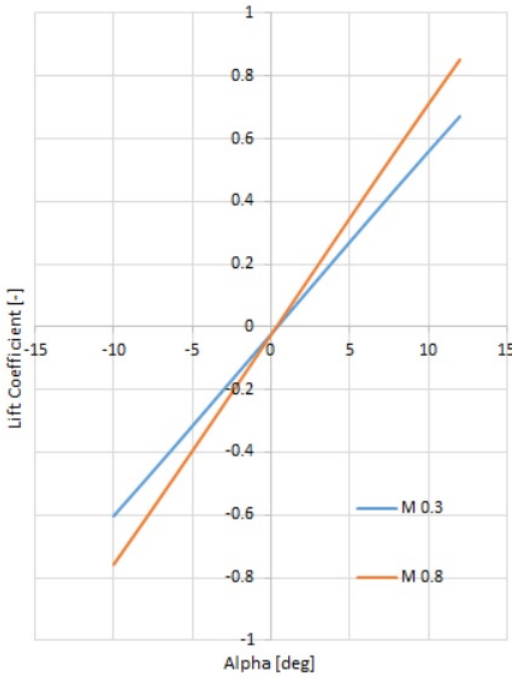

Figure 5.42: Lift Coefficient vs AoA for NASA N3-X

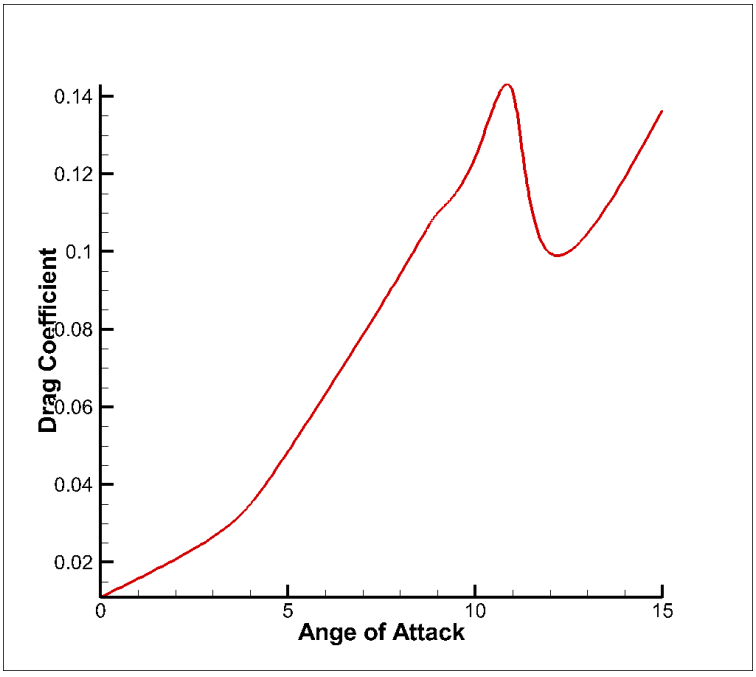

Figure 5.43: Drag Coefficient vs AoA for Inviscid Flow

Table 5.3: Aerodynamic Coefficients for Visocous Flow

Angle of - Attack $(^\circ)$	**Lift Force** (N)	**Coefficient of Lift**	**Drag Force**(N)	**Coefficient of Drag**
0°	744,413	0.165	61,125	0.013
3°	1,642,467	0.366	116,147	0.025
5°	2,125,090	0.473	193,696	0.043

different angles of attack. At the cruise condition, there is a 15% decrease in lift generated. The total lift generated should be higher than the weight of the aircraft. The weight of the aircraft is 225,000 kg. Hence to sustain cruise flight one wing should generate 1,102,500 N of lift force. From Table. 5.3, it is calculated that one wing generates 1,642,467 N of lift. So, the preliminary aerodynamic analysis of the BWB design presented in this thesis shows improvement in aerodynamic performance over the conventional aircraft. Therefore, the provided design can be used as the baseline for a detailed aerodynamic investigation by adding the engines, flight control surfaces, and landing gear.

Conclusion and Future Research

The goals and objectives set for the thesis have been achieved. A BWB aircraft based on the design of the NASA N3-X was created, and aerodynamic analysis was performed. NASA N3-X is a revolutionary aircraft not just from an aerodynamics point of view but also for the propulsion systems, control surfaces, noise reduction, and boundary layer manipulation. Exceptionally few BWB aircraft have been designed and analyzed considering these technologies. The conceptual BWB also considers the current aircraft demands - a midsize passenger aircraft with more extended range and suitable for most airports without any modifications. The conceptual design in this thesis was much inspired by the NASA N3-X to consider these demands.

In this thesis, a BWB aircraft is designed using NACA-23012 and NASA SC(2) - 0606 airfoils. The outer dimensions on the aircraft were similar to N3-X. The length of the aircraft is 41 m, and the span is 64.9 m. The BWB wingspan is almost equal to the Boeing 777 (B777) and hence can operate at all airports that accommodate the B777. The aircraft is shorter by 22 m compared to the B777. The aircraft meshed, and aerodynamic analysis performed using ANSYS Fluent. For saving computation time, a half model was used for simulation.

The BWB configuration was simulated using inviscid flow and a $k-\omega$ SST turbulent model using cruise altitude conditions. The simulations were performed for varying angles of attack. The pressure and Mach number contours were studied to understand the aerodynamics of the aircraft. For the inviscid flow, the maximum lift coefficient was 0.833 at 11°

of attack. The lift shows a gradual increase until it reaches the stall angle after which there is a sharp drop. The drag also shows a linear increase with the angle of attack. The BWB configuration achieved a higher L/D (16.12) compared to the Airbus 380. This proves that BWB configuration has better aerodynamic features compared to the conventional aircraft

For viscous flow, the analysis was performed only till 5° of attack. This was decided based on the fact that aircraft in cruise flight doesn't have a high angle of attack. The results show the same increase in lift forces as shown in inviscid flow. Comparing the results of viscous and inviscid flow, we observe that lift decreases for the viscous flow analysis. This is expected since the boundary layer effect close to the aircraft wall leads to a decrease in lift forces. The viscous flow analysis takes 2.5 - 3 times more computational time as compared to the inviscid flow analysis. Hence the inviscid flow results can be useful for the initial study of the aircraft aerodynamics and to improve the model and the geometry before the final model is created.

The velocity and the pressure contours show that velocity is higher on the top surface corresponding to the decrease in pressure and the velocity is lower at the bottom surface; thus the higher pressure. As the angle of attack is increased the magnitude and intensity of the pressure reduction also increases. The standard shock is also visible especially on the outer wing with variation in the angle of attack. The shock intensity increases, and it moves further towards the leading edge with an increasing angle of attack. The aftershock region, near the aircraft surface, shows signs of reverse flow and flow separation. The flow attaches itself to the surface further downstream. The aftershock region increases as the angle of attack is increased, eventually leading for the flow to be permanently separated causing total loss of lift. This leads to the aircraft stalling. The shock effects are more clearly visible towards the outer wing.

Although the aerodynamic simulation shows that the aircraft is capable of flight, further analysis is needed. One of the primary areas of further research would be to simulate the flow with the control surfaces operational. This will lead to more accurate aerodynamic

lift and drag profile. The aircraft performs many maneuvers during flight - turn, roll and climb. It would be of importance to understand the forces acting on the aircraft surface and how the lift coefficient and drag coefficient vary during these maneuvers. It is recommended that propulsor fans are modeled and study needs to be conducted to understand the effects BLI will have on the overall aircraft performance. A detailed 3D model on the aircraft needs to be created taking the control surface, landing gear, propulsor fans, and turbogenerators. Aerodynamic analysis of detail model needs to be performed at various flight stages namely takeoff, climb, cruise, descent, and landing.

Bibliography

[1] ”airplane concepts” [online]. Available: https://www1.grc.nasa.gov/aeronautics/hep/airplane-concepts/. Accessed: 2019-04-10.

[2] ”ansys fluent guide - 25.1.1 pressure based solver” [online]. Available: https://www.sharcnet.ca/Software/Fluent6/html/ug/node987.htm. Accessed: 2019-04-22.

[3] ”black and white b-2” [online]. Available: https://www.whiteman.af.mil/News/Art/igphoto/2000461437/. Accessed: 2019-04-22.

[4] ”boeing x-48 blended wing body drone” [online]. Available: https://www.militaryfactory.com/aircraft/detail.asp?aircraft_id=1338#variants/. Accessed: 2019-04-10.

[5] ”boeing x-48 unmanned aerial vehicle” [online]. Available: https://www.aerospace-technology.com/projects/boeing-x48-unmanned-aerial-vehicle/. Accessed: 2019-04-10.

[6] ”experimental flying wing aircraft aw.52t” [online]. Available: https://www.militaryfactory.com/aircraft/detail.asp?aircraft_id=1238. Accessed: 2019-04-10.

[7] ”northrop prototype ’avon1’ x216h” [online]. Available: http://www.flightgraphics.com/grand-central/northrop-prototype-avon1.html. Accessed: 2019-04-22.

[8] ”shear-stress transport (sst) k-w model” [online]. Available: https://www.sharcnet.ca/Software/Fluent6/html/ug/node487.htm. Accessed: 2019-04-22.

[9] Hashim Abada. ”turboelectric distributed propulsion system for nasa next generation aircraft.”. Master’s thesis, Wright State University, 2017.

[10] Saif Al-Agele. ”electrical power and storage for nasa next generation aircraft”. Master’s thesis, Wright State University, 2017.

[11] Giancarlo Alfonsi. ”reynolds-averaged navier-stokes equaations for turbulence modeling”. *Applied Mechanics Reviews*, 62:96 – 110, 2009.

[12] Baig AZ, Cheema TA, Aslam Z, Khan YM, Sajid Dar H, and Khaliq SB. ”a new methodology for aerodynamic design and analysis of a small scale blended wing body”. *Journal of Aeronautics Aerospace Engineering*, 7 Issue 1:1 – 6, 2018.

[13] Philippe Ballarini. ”horten two brothers, one wing” [online]. Available: http://aerostories.free.fr/constructeurs/horten/page2.html. Accessed: 2019-04-10.

[14] Joseph R. Chambers. ”innovation in flight”. *NASA Langley Research Center*, pages 71 – 92, 2005.

[15] Payam Dehpanah and Amir Neja. ”the aerodynamic design evaluation of a blended-wing-body configuration”. *Aerospace Science and Technology*, 43 (2015):96 – 110, 2015.

[16] Simon Durrer. ”aerodynamics of race car wing: A cfd study”. Master’s thesis, Grand Valley State University, 2016.

[17] Toshihiro Ikeda. ”aerodynamic analysis of a blended-wing-body aircraft configuration”. Master’s thesis, RMIT University, 2006.

[18] Edward Jones, Adam Littler, and Adam Troughton. ”preliminary design study: Final technical report” volume 1.

[19] F. R. Menter. ”two-equation eddy-viscosity turbulence models for engineering application”. *AIAA Journal*, 32(8):1598 – 1605, 1994.

[20] n.d. ”flying wings” [online]. Available: http://http://www.ctie.monash.edu.au/hargrave/northrop.html#top. Accessed: 2019-04-10.

[21] n.d. ”northrop yb-49” [online]. Available: https://www.nationalmuseum.af.mil/Visit/Museum-Exhibits/Fact-Sheets/Display/Article/858861/northrop-yb-49/. Accessed: 2019-04-10.

[22] n.d. ”statista - estimated annual growth rates for passenger air traffic from 2018 to 2037, by region” [online]. Available: https://www.statista.com/statistics/269919/growth-rates-for-passenger-and-cargo-air-traffic/. Accessed: 2019-04-10.

[23] n.d. ”statista - size of aircraft fleets by region worldwide in 2017 and 2037 (in units)” [online]. Available: https://www.statista.com/statistics/262971/aircraft-fleets-by-region-worldwide//. Accessed: 2019-04-10.

[24] n.d. ”too far, too fast” [online]. Available: https://airscapemag.com/2014/12/18/the-aw52/. Accessed: 2019-04-10.

[25] Stanley Spooner. ”the remington-burnelli ”airliner” twin engine commercial biplane”. *Flight - The Aircraft Engineer and Airships*, 657 (No.30, Vol. 13):505 – 507, 1921.

[26] William Haller and Mark Guynn. ”technical challenges to systems analysis and mdao for advanced subsonic transport aircraft”. URL: https://ntrs.nasa.gov/archive/nasa/casi.ntrs.nasa.gov/20150010336.pdf, 1 2012.

[27] E. T. Woolridge. ”the northrop bombers” [online]. Available: http://www.century-of-flight.net/Aviation%20history/flying%20wings/Northrop%20bombers.html. Accessed: 2019-04-10.